TECHNISCHE UNIVERSITÄT WIEN

AUTOMATION & CONTROL INSTITUTE
INSTITUT FÜR AUTOMATISIERUNGS- & REGELUNGSTECHNIK

Spectral shaping and bifurcation suppression for pulsed laser amplifiers

DIPLOMA THESIS

Conducted in partial fulfillment of the requirements for the degree of a

Diplom-Ingenieur (Dipl.-Ing.)

supervised by

Univ.-Prof. Dr. techn. A. Kugi
Dr. techn. A. Deutschmann-Olek

submitted at the

TU Wien
Faculty of Electrical Engineering and Information Technology
Automation and Control Institute

by
Nikolaus Würkner
Matriculation number 01611813

Vienna, September 2022

Complex Dynamical Systems Group
A-1040 Wien, Gußhausstr. 27–29, Internet: https://www.acin.tuwien.ac.at

Preamble

First and foremost I want to thank my supervisor Dr. Andreas Deutschmann for his unrelenting support and endless patience with any questions and problems that emerged during the development of this thesis, as well as laying the groundwork for this thesis in his PhD thesis. In addition to this I want to thank Prof. Dr. Andreas Kugi, who was always interested in the progress of this thesis and ever helpful with his wealth of knowledge regarding nonlinear systems and their control. This thesis would not have been possible without their support as well as the contributions of my colleagues Philipp Rosenzweig and Lukas Tarra. A special thank you also goes out to my girlfriend Verena for keeping me company during long hours spend at home, programming and fixing the code underlying this thesis, during lockdown. Finally I also want to thank all the members of my family who were ever interested in my progress on this thesis and helped with their own experience in writing scientific work.

Vienna, September 2022

Abstract

Lasers are a flexible and powerful tool in many modern technological and scientific applications. A special type of lasers used in these applications are high-energy pulsed lasers, which need special optical amplifiers to achieve the required energy levels. Among these amplifiers are regenerative amplifiers (RA), which use multiple passes through a gain medium to amplify incoming seed pulses. RAs can show bifurcation due to the coupling of subsequent pulses introduced by the dynamics of the stored energy of the amplifier, which is undesirable for most applications. A control oriented reduced-order mathematical model of such an amplifier is investigated in this thesis in order to suppress these bifurcations using model-based control methods. This model uses small gain estimations of the individual passes through the gain medium combined with slowly varying envelope estimates and spatial averaging to achieve a simplified state-space model of the observed dynamics. Based on this description, a linear quadratic regulator (LQR) combined with an extended Kalman filter (EKF) is designed. The suppression of bifurcations due to feedback stabilization achieved by the LQR then enables the use of output pulse shaping techniques using iterative learning control (ILC) at arbitrary operating points. The designed system is shown to achieve pulse shaping for different operating points while staying within the input constraints introduced by the optical filter.

Kurzzusammenfassung

In vielen wissenschaftlichen und industriellen Anwendungen hat sich der Laser als wichtige und flexible Komponente von vielen modernen Prozessen etabliert. Eine spezielle Variante dieser Laser ist der hoch-energetische, gepulste Laser. Um einen solchen Laser zu erzeugen, sind spezielle optische Verstärker notwendig. Häufig werden hierfür regenerative Verstärker (RA) verwendet welche mehrere Verstärkungszyklen durch das selbe Verstärkungsmedium nutzen um sehr hohe Verstärkungswerte zu erzeugen. Diese Verstärker zeigen Bifurkationen an Betriebspunkten mit starker Kopplung zwischen aufeinanderfolgenden Pulsen aufgrund der unterlagerten Dynamik der gespeicherten Energie. In den meisten Anwendungen ist dies unerwünscht, da es zu einer ungleichmäßigen Energieübertragung führen kann. Ein regelungs-orientiertes reduziertes mathematisches Modell, welches dieses Verhalten reproduzieren kann und in weiterer Folge fÃ¼r den Reglerentwurf genutzt. Basierend auf diesem Modell wurde ein ein LQR (linear quadratic regulator) Entwurf durchgefÃ¼hrt und mit einem erweiterten Kalman-Filter (EKF) kombiniert, um die Bifurkationen zu unterdrücken. Diese Unterdrückung der Bifurkationen kann nun genutzt werden, um modellbasierte iterativ lernende (ILC) Regelung anzuwenden und damit eine spektrale Pulsformung zu ermöglichen. Das implementierte System wurde für verschiedene Arbeitspunkte getestet und zeigt erfolgreiche Unterdrückung der Bifurkationen und eine gewÃ¼nschte Pulsformung innerhalb der Beschränkungen des optischen Filters.

Contents

List of Figures

List of Tables

1 Introduction

The development of the first lasers in the 1950s and 1960s marked a breakthrough for modern optics and quantum physics [1]. Their spatial coherence and narrow frequency band enable their usage in a wide range of fields. These include medical applications (e.g., eye surgery [2]), manufacturing (e.g., laser ablation [3], cutting [4], drilling [5]), scientific research (e.g., nuclear fusion [6], interferometry [7]) and communication (e.g., fiber-optic [8] and free-space optical communication [9]). Many of these applications benefit from high-energy laser pulses compared to continuous wave operation.

A standard approach to obtain high-energy laser pulses is to amplify existing seed pulses (e.g., from a mode-locked laser) to desired energy levels. Typical for the amplification of ultra short high-energy pulses are regenerative amplifier (RA) and related chirped pulse amplifiers (CPAs). RAs use multiple passes through a gain medium to achieve high pulse energy gain [10]. This is generally done by placing the medium inside a resonator cavity. CPAs augment RAs by using a temporal stretcher/compressor scheme to achieve very short pulses without damaging the optical medium with their high energy densities [11]. Both amplifiers deplete their gain capacity, represented by the population inversion of the gain medium, during these passes, which needs to be regenerated in between the amplification of consecutive pulses. If this depletion is not compensated by the regeneration before the next pulse arrives, subsequent pulses are dynamically coupled by the amplifier. This can lead to the amplifier jumping between two or more distinct output pulse energies for equal input pulses or even display chaotic behavior [12]. Behavior like this is called bifurcation and is undesirable for most applications, because they require equal power being delivered with each pulse.

1.1 Pulse shaping

For some applications, not only the amount of energy but also the spectral distribution of the field quantities inside the pulse needs to be adjusted. This is done in a process called pulse shaping [13] using spectral optical filters (e.g., spatial light modulators [14], acousto-optic modulators [15] and deformable mirrors [16]). While such filters can only decrease the total pulse energy, a pulse shaping filter can be combined with an amplifier (e.g., an RA) to generate high-energy pulses with arbitrary spectral profile [17] by accounting for the spectral distribution due to the amplifier. Because of the nonlinear properties of the amplification process, such prefilters need to be adapted for each operating point.

In general, control methods applied to pulse shaping tasks use model-free concepts, such as genetic algorithms [18] or extremum-seeking [19] [20] as well as model-free iterative learning control (ILC) variants [21]. This is justified by the highly complex effects the nonlinear distributed-parameter system displays, as well as the degree of uncertainty which is inherent to some parameters of the system. Some work has been done on using

an ILC-based approach on single-pass and double-pass amplifiers [21]. Recent work has also extended ILC approaches to multi-pass chirped pulse amplifiers [22], which, due to their high gain values and spectrally inhomogeneous saturation, are more challenging. Some remaining open questions of this paper sparked interest in the research done in this thesis. These chirped pulse amplifiers are typically operated in a regime at high pulse repetition rates with coupling of consecutive pulses, the effects of which have been discussed previously. Since this coupling can lead to bifurcation and therefore unstable operation, the adaptive strategy presented in the previous work needed to be limited to stable operating points. This thesis aims at developing a model to reproduce this coupling behavior, applying model-based control concepts to stabilize it and using model-based ILC methods for pulse shaping at these stabilized operating points.

1.2 Iterative learning control

For systems working in a repetitive mode, iterative learning control (ILC) offers a systematic approach to reduce the tracking error of desired output quantities [23]. This is done by adapting the input values $\mathbf{u}_{i+1}$ of iteration $i+1$ based on the measured tracking error of the previous iteration i. A typical linear update law used for ILCs is

$$\mathbf{u}_{i+1} = \mathbf{u}_i + \mathbf{L}_i(\mathbf{y}_d - \mathbf{y}_i), \tag{1.1}$$

with the input values $\mathbf{u}_{i+1}$ and $\mathbf{u}_i$, the learning operator $\mathbf{L}_i$, as well as the desired and measured output quantities $\mathbf{y}_d$ and $\mathbf{y}_i$. This law is frequently augmented using an operator $\mathbf{Q}$, which can be used to suppress the influence of disturbances and increase robustness. This leads to the modified update law

$$\mathbf{u}_{i+1} = \mathbf{Q}\Big(\mathbf{u}_i + \mathbf{L}_i(\mathbf{y}_d - \mathbf{y}_i)\Big). \tag{1.2}$$

There are a multitude of different methods available to design the learning parameter $\mathbf{L}$ and the filter $\mathbf{Q}$. Among these are very simple methods such as P-Type ILCs using a constant $\mathbf{L}$ parameter. In [24], $L = k_p\,\mathbf{I}$ is employed, with the constant k_p and the identity operator $\mathbf{I}$, for tracking control of a nonlinear systems. A combination of this proportional component with a differential component $k_d\,\mathbf{D}$, with a constant k_d and a derivative operator $\mathbf{D}$, results in PD-Type ILCs. An example of such a system is given in [25] for servo control of a permanent magnet synchronous motor. More complex ILC variants follow an inversion-based approach, which inverts the connection between the input values u_i to the output values y_i and uses this as the learning operator $\mathbf{L}$. Often some kind of optimization approaches are utilized to calculate an approximate inversion Examples for this can be found in [26] for over-actuated systems and in [27] using a pseudo-inverse approach.

There are also multiple ways to design $\mathbf{Q}$ [28]. Many of these filters are designed to feature a low-pass characteristic [29]. This leads to high-frequency components of the error not being learned, which in general leads to better rejection of noise and high frequency disturbances and ensures the stability of the ILC. For specific applications, band-pass characteristics might also be useful to reject given disturbances.

1.3 Structure of this thesis

Since this thesis aims to develop model-based control methods for regenerative amplifiers that combine bifurcation suppression and pulse-shaping strategies, Chapter 2 starts with the development of reduced-order mathematical models. A complex, nonlinear and distributed-parameter model of the amplifier is shortly introduced and serves as a reference for all further simulations. Based on this reference model, two submodels are derived, with the first modeling the amplification due to a single pass through the medium and the resulting depletion in population, and the second model capturing the regeneration of the population inversion during the regeneration phases between two pulses. These two submodels can be combined to a full model of the pulse amplification and population dynamics of an RA, which also covers the coupling of subsequent pulses, i.e., the pulse-to-pulse dynamics. This reduced-order model then needs to be calibrated. In Chapter 3, this is tested for data only available from the simulations of the reference model to establish a baseline, as well as from data which are available from measurements for comparison. The resulting pulse-to-pulse dynamics can be represented in a discrete-time state-space representation. A state feedback controller as well as a state observer are designed for this system in Chapter 4. The feedback controller is based on linearization and solving a linear-quadratic-regulator (LQR) problem. For state estimation an extended Kalman filter is designed in Chapter 4. The combined controller and estimator are used to suppress bifurcations at unstable operating points. This stabilization approach is then combined with an ILC-based pulse-shaping scheme and tested for unstable as well as stable operating points in Chapter 5. Chapter 6 then summarizes the developments and gives an outlook on further extensions of this thesis. In addition to these chapters, the thesis contains an appendix with four subsections. Section A.1 shows the assumptions associated with the slowly varying envelope approximation (SVEA) used in the derivation of the reference model in Chapter 2. A selection of identities for the Fourier transform of a time function is given in Section A.2, which are used in Chapter 2 to derive the reduced-order model. Section A.3 deals with the derivation of the imaginary difference method, which can be used for numerical differentiation and is applied multiple times in this thesis. A detailed description of the steady-state calibration done in Chapter 3 is presented in Section A.4.

2 Mathematical models of regenerative optical amplifiers

In this thesis, a detailed mathematical model which is presented in this chapter is used as a reference to evaluate the performance of the developed control algorithms.

This thesis aims to apply iterative learning control (ILC) to shape the input pulse of the amplifier in order to yield a desired output pulse. These ILC algorithms all use some type of model inversion for their learning iterations. Using the reference model to calculate this inversion is not feasible due to the extremely high numerical effort. Therefore, a model of reduced complexity is needed which can be used for online calculations.

The following sections go through a detailed description of the modeling applied to the regenerative laser amplifier covered in this thesis. Starting with an overview of the basic functionality of a regenerative amplifier a description of the equations used in the reference model analogous to [22] is given. Based on these equations, the reduced-order model is derived afterwards. The two models are then compared in the last section.

2.1 Reference model of the regenerative amplifier

Regenerative optical amplifiers (RA) use multiple passes through an active laser medium to achieve high-gain values, a schematic overview of this is presented in Figure 2.1. Once the energy stored in the medium is depleted, the pulse is released. The energy is replenished by a constant stream of pumping light, regenerating the gain available for the next pulse. A special type of RA is the chirped pulse amplifier (CPA), which uses an optical stretcher and a compressor to avoid damaging the optical components due to the atomic energy density of ultra-short pulses. For simplicity, we will restrict ourselves to RAs in this thesis, although the developed algorithms can be directly applied to CPAs.

A Holmium-doped yttrium aluminum garnet (Ho:YAG) is used in the amplifier. This type of solid-state medium features five resonant transitions in the mid-infrared region. A simple energy level diagram and the coupling transitions are shown in Figure 2.2.

Any electromagnetic wave propagating through the crystal interacts with the population densities N_j of the different energy levels. Photons with energies matching the energy level differences can trigger stimulated emission or be absorbed. Stimulated emission is when the photon interacts with an ion at the higher energy state and releases an additional photon with the same energy, effectively doubling the amount of photons. During absorption, the photon interacts with a ion on the lower energy level, raising it to the higher level, with the photon being absorbed in the process. A typical pulse inside the RA at $1,5\text{mJ}$ is made up of about 16 quadrillion individual photons. The interaction of any single photon is irrelevant, it is only of interest whether the amount of photons is increased or reduced for a frequency. Interactions with either of the energy levels are

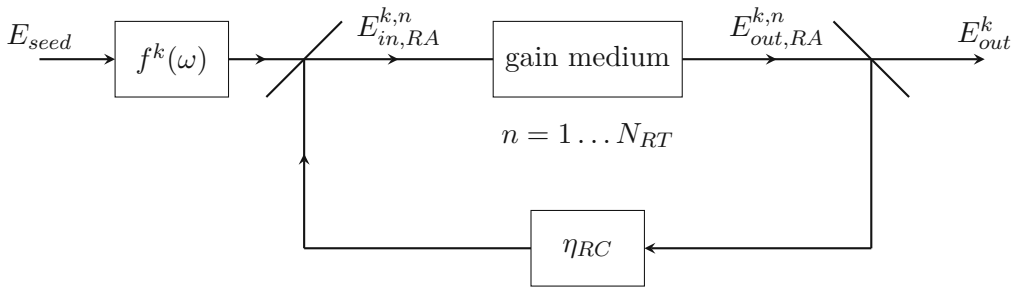

Figure 2.1: Layout of the regenerative amplifier, with the input filter $f^k(\omega)$ generating the k-th initial input pulse $E^{k,0}_{in,RA}$. It enters the setup, gets amplified by the gain medium, and then reflected by the resonator mirror. The round-trip losses η_{RC} represent all losses during the return trip of the pulse. After a set amount of round-trips, the pulse is released as the k-th output pulse E^k_{out}

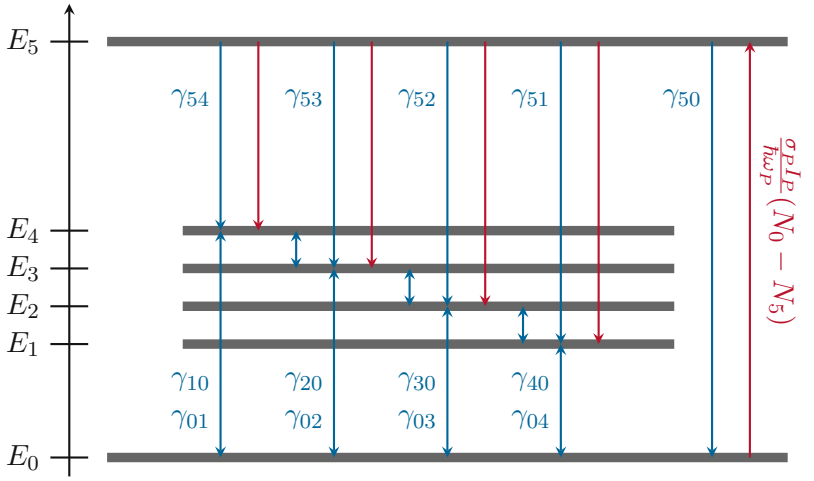

Figure 2.2: Simple energy level diagram for the Ho:YAG, with all five resonant transitions in red and eleven radiative as well as non-radiative relaxation transitions in blue.

more likely if its associated population is higher. On average, more stimulated emission will happen if the population difference between the higher and the lower energy level, called the inversion, is positive. Otherwise absorption will be dominant.

The non-radiative transitions also present inside the crystal work differently. Interactions along these are either spontaneous in nature or triggered by phononic excitation of the crystal. Spontaneous lattice non-radiative interactions lead to an ion dropping from a higher to a lower energy level, releasing a phonon into the crystal. The ones triggered by a phonon absorb it and raise an ion to the higher energy level. These transitions are qualified by their relaxation probabilities γ_{ij}.

As discussed above, the amplification of an optical pulse is driven by stimulated emission of photons, which is dominant if the population inversion is positive. Therefore inversion needs to be built up in any radiating transitions used for amplification. This is done by exciting a large amount of ions to the higher energy level. In the Ho:YAG medium this is E_5. This excitation is typically done by using one of the radiative transitions, shining a continuous beam of high intensity light of its frequency at the crystal, a process called optical pumping. The laser modeled in this thesis uses the transition between E_0 and E_5 for pumping. To quantify the strength of this pumping light its intensity I_P is used.

Every pulse propagating through the gain medium can be described by two field quantities, the electric field strength E and the atomic polarization P of the doped ions, both of which are complex quantities distributed over time and space. Since four resonant transitions are used for Ho:YAG media, P can be split into four polarization contributions P_1, P_2, P_3, P_4. As is typical for laser applications over relatively short propagation distances, the pulse can be represented using plane waves. Setting the axis z on the propagation direction and assuming a homogeneous transversal profile, a field quantity can be written in envelope representation as

$$\mathcal{A}(z,t) = A(z,t)e^{-i(k_0 z-\omega_0 t)},$$

with the time t, the spatial coordinate z, the imaginary unit i, the central angular frequency ω_0, the corresponding spatial wave number k_0 and the complex pulse envelope $A(z,t)$. In the following derivations, the time, space and frequency dependence of field quantities is omitted, unless needed for better understanding. All spatial and temporal variations of the pulse envelope are assumed slow compared to the carrier frequency, using the slowly varying envelope approximation (SVEA). An overview of the approximations is given in Section A.1.

Using these approximations yields the polarization-driven nonlinear Schrödinger equation [22]

$$i\frac{\partial E}{\partial z} + \frac{k_2}{2}\frac{\partial^2 E}{\partial t^2} - \frac{1}{2}\omega_0\varepsilon_0 n_0 n_2 |E|^2 E = \frac{\omega_0^2}{2c_0\varepsilon_0 k_0}(P_1 + P_2 + P_3 + P_4) \tag{2.3a}$$

together with the resonant dipole equation [22]

$$\frac{\partial P_j}{\partial t} = -\frac{\omega_j^2 + j\omega_0\Delta\omega_j - \omega_0^2}{\Delta\omega_j + 2i\omega_0}P_j + \frac{\kappa_j}{\Delta\omega_j + 2i\omega_0}(N_j - N_5)E, \qquad j = 1,\dots,4, \tag{2.3b}$$

and the associated population dynamic [22]

$$\frac{\partial N_1}{\partial t} = \frac{1}{2\hbar}\mathrm{Im}\Big\{E^* P_1\Big\} - (\gamma_{10}+\gamma_{12})N_1 + \gamma_{21}N_2 + \gamma_{51}N_5 + \gamma_{01}N_0 \tag{2.3c}$$

$$\frac{\partial N_2}{\partial t} = \frac{1}{2\hbar}\mathrm{Im}\Big\{E^* P_2\Big\} + \gamma_{12}N_1 - (\gamma_{20}+\gamma_{20}+\gamma_{23})N_2 + \gamma_{32}N_3 + \gamma_{52}N_5 + \gamma_{02}N_0 \tag{2.3d}$$

$$\frac{\partial N_3}{\partial t} = \frac{1}{2\hbar}\mathrm{Im}\Big\{E^* P_3\Big\} + \gamma_{23}N_2 - (\gamma_{30}+\gamma_{32}+\gamma_{34})N_3 + \gamma_{43}N_4 + \gamma_{53}N_5 + \gamma_{03}N_0 \tag{2.3e}$$

$$\frac{\partial N_4}{\partial t} = \frac{1}{2\hbar}\mathrm{Im}\Big\{E^* P_4\Big\} + \gamma_{34}N_3 - (\gamma_{40}+\gamma_{43}+\gamma_{45})N_4 + \gamma_{54}N_5 + \gamma_{04}N_0 \tag{2.3f}$$

$$\frac{\partial N_5}{\partial t} = -\frac{1}{2\hbar}\mathrm{Im}\Big\{E^* \sum_{j=1}^{4} P_j\Big\} - (\gamma_{50}+\gamma_{51}+\gamma_{52}+\gamma_{53}+\gamma_{54})N_5 + \frac{\sigma I_P}{\hbar\omega_P}(N_0 - N_5). \tag{2.3g}$$

The equation for the spatial distribution of the pumping intensity is given by

$$\frac{\partial I_P}{\partial z} = \sigma_P(N_5 - N_0)I_P. \tag{2.3h}$$

Here the spectral dependence of the wave number is represented by k_2, c_0 is the speed of light, μ_0 the permeability of free space, ε_0 the permittivity of free space and $\hbar$ is the reduced Plank constant. The parameters ω_j and $\Delta\omega_j$ are the resonant frequency and spectral width for the resonant transition $5 \leftrightarrow j$, respectively. In addition $\kappa_j = \frac{\omega_j \varepsilon_0 c_0 \Delta\omega_j \sigma_j}{\omega_0}$ with the transition cross section σ_j, is used as shorthand. The population dynamics uses the direct relaxation probability γ_{ij} for the transition $i \leftrightarrow j$, the local pumping field intensity $I_P(z,t)$, the pumping field's cross section σ_P and its angular frequency ω_P. Equation (2.3a) represents the influence of the polarization on the electric field and linear and nonlinear effects during the propagation of the pulse. The resonant dipole equations represent the dynamic of the polarization due to the population inversions of the resonant transitions. There is no extra equation for the ground level population density N_0 because the sum of all population densities is equal to the dopant density, i.e.

$$N_0 + N_1 + N_2 + N_3 + N_4 + N_5 = N_{dop}. \tag{2.4}$$

For a more detailed derivation of these equations, see [22]. The simulation model using (2.3) was calibrated to closely match the measurements of an experimental amplifier.

The set of equations in (2.3) offer a very detailed model of a single pulse's amplification. The full model of the amplifier is then given by successive application of the model (2.3) for each round trip while considering losses in between, see [22]. The distributed characteristics of (2.3) in space and time is challenging for numerical evaluations, leading to very long computation-times. Hence, it is not feasible for real-time applications using model-based methods. For these applications, a different model needs to be derived.

2.2 Small gain approximation of pulse propagation

As discussed previously, regenerative amplifiers feature relatively small pulse gain values during one propagation through the gain medium. Since any energy added to the pulse is

balanced by a reduction of the population inversion, the change in population during one propagation can also be assumed small. We can therefore assume that the gain during one propagation is not changed significantly if we keep the population inversion constant

$$N_j(z,t) = N_j(z,0) = N_j^0(z). \tag{2.5}$$

Using this assumption and neglecting the nonlinear components, (2.3a) and (2.3b) can be written as

$$i\frac{\partial E}{\partial z} = -\frac{k_2}{2}\frac{\partial^2 E}{\partial t^2} + \frac{\omega_0^2}{2c_0\varepsilon_0 k_0}(P_1 + P_2 + P_3 + P_4) \tag{2.6a}$$

and

$$\frac{\partial P_j}{\partial t} = -\frac{\omega_j^2 + j\omega_0\Delta\omega_j - \omega_0^2}{\Delta\omega_j + 2i\omega_0}P_j - \frac{\kappa_j}{\Delta\omega_j + 2i\omega_0}(N_5^0 - N_j^0)E. \tag{2.6b}$$

This now makes it possible to apply the Fourier transform to both equations. Using (A.99), this results in

$$i\frac{\partial \hat{E}}{\partial z} = \frac{k_2}{2}\omega^2\hat{E} + \frac{\omega_0^2}{2c_0\varepsilon_0 k_0}(\hat{P}_1 + \hat{P}_2 + \hat{P}_3 + \hat{P}_4) \tag{2.7a}$$

and

$$i\omega\hat{P}_j = -\frac{\omega_j^2 + j\omega_0\Delta\omega_j - \omega_0^2}{\Delta\omega_j + 2i\omega_0}\hat{P}_j - \frac{\kappa_j}{\Delta\omega_j + 2i\omega_0}\Delta N_{5j}^0\hat{E}, \tag{2.7b}$$

with the initial population inversion $\Delta N_{5j}^0 = N_5^0 - N_j^0$. Note that all quantities in the Fourier space are represented with a hat, e.g.

$$\hat{A}(z,\omega) = \mathcal{F}[A(z,t)](\omega). \tag{2.8}$$

Solving the resulting linear set of differential and algebraic equations for $\hat{E}$ and $\hat{P}_j$ yields

$$\hat{P}_j = \frac{-\kappa_j\Delta N_{5j}^0}{\omega_j^2 + i\omega(\Delta\omega_j + 2i\omega_0) + i\omega_0\Delta\omega_j - \omega_0^2}\hat{E} = \chi_j(\omega, \Delta N_{5j}^0)\hat{E}, \tag{2.9a}$$

with the electric susceptibility χ_j and

$$\hat{E}(z,\omega) = \exp\Big[-i\int_0^z \frac{k_2}{2}\omega^2 + \frac{\omega_0^2}{2c_0^2\varepsilon_0 k_0}\sum_{j=1}^4 \chi_j(\omega, \Delta N_{5j}^0)dz\Big]\hat{E}_{in,RA}(\omega). \tag{2.9b}$$

Since the electric susceptibility is linear with respect to the population inversion, we can solve the integral by using the mean population $\Delta\bar{N}_{5j}^0 = \frac{1}{L}\int_0^L N_{5j}^0(z)dz$. Evaluating (2.9b) at the length L of the crystal, yields the pulse exiting the gain medium

$$\begin{aligned}\hat{E}_{out,RA}(\omega) &= \exp\Big[-iL\Big(\frac{k_2}{2}\omega^2 + \frac{\omega_0^2}{2c_0^2\varepsilon_0 k_0}\sum_{j=1}^4 \chi_j(\omega, \Delta\bar{N}_{5j}^0)\Big)\Big]\hat{E}_{in,RA}(\omega) \\ &= \underline{G}(\omega, \bar{\mathbf{N}}^0)\hat{E}_{in,RA}(\omega),\end{aligned} \tag{2.10}$$

with the complex gain spectrum $\underline{G}(\omega, \mathbf{N}^0)$, using the vector of the population densities

$$\mathbf{N} = \left[N_1, N_2, N_3, N_4, N_5\right]^{\mathrm{T}}. \tag{2.11}$$

This gain can be split into an absolute component

$$G(\omega, \mathbf{N}^0) = \exp\left[L\left(\frac{\omega_0^2}{2c_0^2\varepsilon_0 k_0}\sum_{j=1}^{4}\mathrm{Im}\left\{\chi_j(\omega, \Delta\bar{N}_{5j}^0)\right\}\right)\right] \tag{2.12a}$$

and a phase component

$$\varphi_G(\omega, \mathbf{N}^0) = -\frac{k_2 L}{2}\omega^2 - \frac{\omega_0^2 L}{2c_0^2\varepsilon_0 k_0}\sum_{j=1}^{4}\mathrm{Re}\left\{\chi_j(\omega, \Delta\bar{N}_{5j}^0)\right\}. \tag{2.12b}$$

We now know that we need the mean initial population at the beginning of the propagation for a good estimate of the pulse gain. The following section derives a method to calculate the population change during the propagation of one pulse through the gain medium in order to calculate this mean initial population for each propagation.

2.3 Population dynamic during the propagation

This population change is based on the population dynamics of the reference model in (2.3c) to (2.3g). The right sides of the equations can be split into two parts, the inversion reduction due to the resonant transitions and the relaxation and pumping component. These two parts work on very different timescales, with the relaxation and pumping being significantly slower than the pulse interaction. Therefore, we can assume that its influence on the population change during one propagation is negligible. This results in the new population dynamics equations

$$\frac{\partial N_1}{\partial t} = \frac{1}{2\hbar}\mathrm{Im}\left\{E^* P_1\right\}, \tag{2.13a}$$

$$\frac{\partial N_2}{\partial t} = \frac{1}{2\hbar}\mathrm{Im}\left\{E^* P_2\right\}, \tag{2.13b}$$

$$\frac{\partial N_3}{\partial t} = \frac{1}{2\hbar}\mathrm{Im}\left\{E^* P_3\right\}, \tag{2.13c}$$

$$\frac{\partial N_4}{\partial t} = \frac{1}{2\hbar}\mathrm{Im}\left\{E^* P_4\right\}, \tag{2.13d}$$

$$\frac{\partial N_5}{\partial t} = -\frac{1}{2\hbar}\mathrm{Im}\left\{E^* \sum_{j=1}^{4} P_j\right\}. \tag{2.13e}$$

We can now calculate the change of population N_1 due to the propagation of one pulse by integrating both sides of (2.13a), yielding

$$\Delta_t N_1(z) = N_{1,end}(z) - N_1^0(z) = \int_{-\infty}^{\infty}\frac{\partial N_1(z,t)}{\partial t}dt \tag{2.14a}$$

$$= \frac{1}{2\hbar}\int_{-\infty}^{\infty}\mathrm{Im}\left\{E^*(z,t)P_1(z,t)\right\}dt. \tag{2.14b}$$

Applying the identity in (A.100), we can replace the right side with the zero frequency component

$$\Delta_t N_1(z) = \frac{1}{2\hbar}\mathcal{F}\Big[\mathrm{Im}\Big\{E^*(z,t)P_1(z,t)\Big\}\Big](\omega)\Big|_{\omega=0}. \tag{2.15a}$$

Due to the linearity of the Fourier transform and the imaginary part, we can rearrange the right side to get

$$\Delta_t N_1(z) = \frac{1}{2\hbar}\mathrm{Im}\Big\{\mathcal{F}\big[E^*(z,t)P_1(z,t)\big](\omega)\Big\}\Big|_{\omega=0}. \tag{2.15b}$$

Applying the identities (A.102) and (A.101) to (2.15b) yields

$$\Delta_t N_1(z) = \frac{1}{2\hbar}\mathrm{Im}\Big\{\int_{-\infty}^{\infty}\hat{E}^*(z,-\omega')\hat{P}_1(z,\omega-\omega')d\omega'\Big\}\Big|_{\omega=0} \tag{2.15c}$$

$$= \frac{1}{2\hbar}\mathrm{Im}\Big\{\int_{-\infty}^{\infty}\hat{E}^*(z,-\omega')\hat{P}_1(z,-\omega')d\omega'\Big\} \tag{2.15d}$$

$$= \frac{1}{2\hbar}\mathrm{Im}\Big\{\int_{-\infty}^{\infty}\hat{E}^*(z,\omega)\hat{P}_1(z,\omega)d\omega\Big\}. \tag{2.15e}$$

Using the definition of the electric susceptibility in (2.9a), we get

$$\Delta_t N_1(z) = \frac{1}{2\hbar}\mathrm{Im}\Big\{\int_{-\infty}^{\infty}\hat{E}^*(z,\omega)\chi_1(\omega,\Delta N_{51}^0)\hat{E}(z,\omega)d\omega\Big\} \tag{2.15f}$$

$$= \frac{1}{2\hbar}\mathrm{Im}\Big\{\int_{-\infty}^{\infty}|\hat{E}(z,\omega)|^2\chi_1(\omega,\Delta N_{51}^0)d\omega\Big\}. \tag{2.15g}$$

The small gain estimate of the pulse amplification only needs the mean value of the initial population for each propagation. Therefore, we apply the spatial mean to the population change to get the change in the mean population

$$\Delta_t \bar{N}_1 = \bar{N}_{1,end} - \bar{N}_1^0 = \frac{1}{L}\int_0^L \Delta_t N_1(z)dz. \tag{2.16a}$$

Using the derivations above, we can write

$$\Delta_t \bar{N}_1 = \frac{1}{2\hbar}\frac{1}{L}\int_0^L\int_{-\infty}^{\infty}|\hat{E}(z,\omega)|^2\mathrm{Im}\Big\{\chi_1(\omega,\Delta N_{51}^0)\Big\}d\omega\ dz. \tag{2.16b}$$

If we assume that the variation of the population is small across the spatial dimension, we can replace ΔN_{5j}^0 with $\Delta\bar{N}_{5j}^0$ and shift the susceptibility out of the spatial integral to get

$$\Delta_t \bar{N}_1 = \frac{1}{2\hbar}\int_{-\infty}^{\infty}\frac{1}{L}\int_0^L|\hat{E}(z,\omega)|^2dz\ \mathrm{Im}\{\chi_1(\omega,\Delta\bar{N}_{51}^0)\}d\omega. \tag{2.16c}$$

Applying the same assumption to the population, we can expect the absolute of the spectral gain in (2.12a) to be of exponential shape in the spatial dimension, meaning

$$|G(\omega,\mathbf{N}^0)| \approx \exp\big[\alpha_G(\omega,\bar{\mathbf{N}}^0)L\big], \tag{2.16d}$$

with

$$\alpha_G(\omega, \bar{\mathbf{N}}^0) = \frac{\omega_0^2}{2c_0^2\varepsilon_0 k_0} \sum_{j=1}^{4} \mathrm{Im}\Big\{\chi_j(\omega, \Delta\bar{N}_{5j}^0)\Big\}. \tag{2.16e}$$

This exponential shape can now be used to calculate the mean squared electric field strength

$$\frac{1}{L}\int_0^L |G|^2 dz = \frac{\exp\big[2\alpha_G(\omega, \bar{\mathbf{N}}^0)L\big] - 1}{2\alpha_G(\omega, \bar{\mathbf{N}}^0)L} \tag{2.16f}$$

and use it to calculate the population change during one propagation depending on the input pulse

$$\Delta_t \bar{N}_1 = \frac{1}{2\hbar}\int_{-\infty}^{\infty} \frac{\exp\big[2\alpha_G(\omega, \bar{\mathbf{N}}^0)L\big] - 1}{2\alpha_G(\omega, \bar{\mathbf{N}}^0)L} |\hat{E}(0,\omega)|^2 \mathrm{Im}\{\chi_1(\omega, \Delta\bar{N}_{51}^0)\} d\omega. \tag{2.16g}$$

We can also calculate this change depending on the pulse after its amplification

$$\Delta_t \bar{N}_1 = \frac{1}{2\hbar}\int_{-\infty}^{\infty} \frac{\exp\big[-2\alpha_G(\omega, \bar{\mathbf{N}}^0)L\big] - 1}{-2\alpha_G(\omega, \bar{\mathbf{N}}^0)L} |\hat{E}(L,\omega)|^2 \mathrm{Im}\{\chi_1(\omega, \Delta\bar{N}_{51}^0)\} d\omega. \tag{2.16h}$$

With the derivation above, the mean population after the propagation of pulse $\hat{E}_{in}(\omega)$, starting at a mean population $\bar{\mathbf{N}}^0$ can now be estimated using

$$\bar{N}_{1,end} = \bar{N}_1^0 + \frac{1}{2\hbar}\int_{-\infty}^{\infty} \frac{\exp\big[2\alpha_G(\omega, \bar{\mathbf{N}}^0)L\big] - 1}{2\alpha_G(\omega, \bar{\mathbf{N}}^0)L} |\hat{E}_{in}(\omega)|^2 \mathrm{Im}\{\chi_1(\omega, \Delta\bar{N}_{51}^0)\} d\omega. \tag{2.17a}$$

Proceeding analogously for the other populations yields

$$\bar{N}_{2,end} = \bar{N}_2^0 + \frac{1}{2\hbar}\int_{-\infty}^{\infty} \frac{\exp\big[2\alpha_G(\omega, \bar{\mathbf{N}}^0)L\big] - 1}{2\alpha_G(\omega, \bar{\mathbf{N}}^0)L} |\hat{E}_{in}(\omega)|^2 \mathrm{Im}\{\chi_2(\omega, \Delta\bar{N}_{52}^0)\} d\omega, \tag{2.17b}$$

$$\bar{N}_{3,end} = \bar{N}_3^0 + \frac{1}{2\hbar}\int_{-\infty}^{\infty} \frac{\exp\big[2\alpha_G(\omega, \bar{\mathbf{N}}^0)L\big] - 1}{2\alpha_G(\omega, \bar{\mathbf{N}}^0)L} |\hat{E}_{in}(\omega)|^2 \mathrm{Im}\{\chi_3(\omega, \Delta\bar{N}_{53}^0)\} d\omega, \tag{2.17c}$$

$$\bar{N}_{4,end} = \bar{N}_4^0 + \frac{1}{2\hbar}\int_{-\infty}^{\infty} \frac{\exp\big[2\alpha_G(\omega, \bar{\mathbf{N}}^0)L\big] - 1}{2\alpha_G(\omega, \bar{\mathbf{N}}^0)L} |\hat{E}_{in}(\omega)|^2 \mathrm{Im}\{\chi_4(\omega, \Delta\bar{N}_{54}^0)\} d\omega, \tag{2.17d}$$

$$\bar{N}_{5,end} = \bar{N}_5^0 - \sum_{j=1}^{4} \frac{1}{2\hbar}\int_{-\infty}^{\infty} \frac{\exp\big[2\alpha_G(\omega, \bar{\mathbf{N}}^0)L\big] - 1}{2\alpha_G(\omega, \bar{\mathbf{N}}^0)L} |\hat{E}_{in}(\omega)|^2 \mathrm{Im}\{\chi_j(\omega, \Delta\bar{N}_{5j}^0)\} d\omega. \tag{2.17e}$$

These equations can now estimate the change of all five populations during the propagation of one pulse. The ground state population N_0 does not experience any population change induced by the pulse. This is easily visible in two ways. Firstly, the population changes in (2.17) cancel each other. Secondly, in Figure 2.2 no resonant transition used for amplification is interacting with the ground state, except for the one used for pumping. With a set of equations to calculate the population change during one propagation, we still need a way to describe the population dynamics between two pulses. A model for this process is derived in the next section.

2.4 Population regeneration between pulses

During phases with no pulse inside the gain medium, the influence of relaxation and pumping on the population density can not be neglected. Taking the population dynamic in (2.3c) to (2.3h) and setting the electric field strength to zero results in

$$\frac{\partial N_1}{\partial t} = -(\gamma_{10} + \gamma_{12})N_1 + \gamma_{21}N_2 + \gamma_{51}N_5 + \gamma_{01}N_0 \tag{2.18a}$$

$$\frac{\partial N_2}{\partial t} = \gamma_{12}N_1 - (\gamma_{20} + \gamma_{21} + \gamma_{23})N_2 + \gamma_{32}N_3 + \gamma_{52}N_5 + \gamma_{02}N_0 \tag{2.18b}$$

$$\frac{\partial N_3}{\partial t} = \gamma_{23}N_2 - (\gamma_{30} + \gamma_{32} + \gamma_{34})N_3 + \gamma_{43}N_4 + \gamma_{53}N_5 + \gamma_{03}N_0 \tag{2.18c}$$

$$\frac{\partial N_4}{\partial t} = \gamma_{34}N_3 - (\gamma_{40} + \gamma_{43} + \gamma_{45})N_4 + \gamma_{54}N_5 + \gamma_{04}N_0 \tag{2.18d}$$

$$\frac{\partial N_5}{\partial t} = -(\gamma_{50} + \gamma_{51} + \gamma_{52} + \gamma_{53} + \gamma_{54})N_5 + \frac{\sigma I_P}{\hbar\omega_P}(N_0 - N_5) \tag{2.18e}$$

and

$$\frac{\partial I_P}{\partial z} = \sigma_P(N_5(z,t) - N_0(z,t))I_P(z,t). \tag{2.18f}$$

As discussed previously, we can expect the population density variation across the spatial dimension to be relatively small, they are therefore replaced by mean population densities $\bar{N}_5$ and $\bar{N}_0$ in (2.18f), yielding

$$\frac{\partial I_P}{\partial z}(z,t) = \sigma_P(\bar{N}_5(t) - \bar{N}_0(t))I_P(z,t), \tag{2.19}$$

which can be solved

$$I_P(z,t) = \exp\Big[\sigma_P(\bar{N}_5(t) - \bar{N}_0(t))\, z\Big] I_p(0,t). \tag{2.20}$$

By using the information in (2.4) about the sum of the population being constant, the pump intensity can be calculated without the need for N_0, i.e.

$$I_P(z,t) = \exp\Big[\sigma_P(\bar{N}_1(t) + \bar{N}_2(t) + \bar{N}_3(t) + \bar{N}_4(t) + 2\bar{N}_5(t) - N_{dop})\, z\Big] I_p(0,t). \tag{2.21}$$

With the vector of mean populations $\bar{\mathbf{N}} = [\bar{N}_1, \bar{N}_2, \bar{N}_3, \bar{N}_4, \bar{N}_5]$, this can be rewritten as

$$I_P(z,t) = \exp\Big[\sigma_P(\Big[1 \quad 1 \quad 1 \quad 1 \quad 2\Big]\bar{\mathbf{N}} - N_{dop})\, z\Big] I_p(0,t). \tag{2.22}$$

By applying (2.4) to (2.18) and rearranging it into a matrix equation, we get

$$\frac{\partial \mathbf{N}}{\partial t} = \mathbf{\Gamma N} + \mathbf{\Gamma}_{dop} N_{dop}, \tag{2.23}$$

with

$$\mathbf{\Gamma} = \begin{bmatrix} \Gamma_{11} & (\gamma_{21}-\gamma_{01}) & -\gamma_{01} & -\gamma_{01} & \gamma_{51}-\gamma_{01} \\ \gamma_{12}-\gamma_{02} & \Gamma_{22} & \gamma_{32}-\gamma_{02} & -\gamma_{02} & \gamma_{52}-\gamma_{02} \\ -\gamma_{03} & \gamma_{23}-\gamma_{03} & \Gamma_{33} & \gamma_{43}-\gamma_{03} & \gamma_{53}-\gamma_{03} \\ -\gamma_{04} & -\gamma_{04} & \gamma_{34}-\gamma_{04} & \Gamma_{44} & -\gamma_{04} \\ -\frac{\sigma I_P(z,t)}{\hbar\omega_P} & -\frac{\sigma I_P(z,t)}{\hbar\omega_P} & -\frac{\sigma I_P(z,t)}{\hbar\omega_P} & -\frac{\sigma I_P(z,t)}{\hbar\omega_P} & \Gamma_{55}(I_P(z,t)) \end{bmatrix}, \mathbf{\Gamma}_{dop} = \begin{bmatrix} \gamma_{01} \\ \gamma_{02} \\ \gamma_{03} \\ \gamma_{04} \\ \frac{\sigma I_P(z)}{\hbar\omega_P} \end{bmatrix}$$

$$\Gamma_{11} = -(\gamma_{10}+\gamma_{12}+\gamma_{01}), \qquad \Gamma_{22} = -(\gamma_{20}+\gamma_{21}+\gamma_{23}+\gamma_{02}),$$
$$\Gamma_{33} = -(\gamma_{30}+\gamma_{32}+\gamma_{34}+\gamma_{03}), \qquad \Gamma_{44} = -(\gamma_{40}+\gamma_{43}+\gamma_{45}+\gamma_{04}),$$

$$\Gamma_{55}(z,t) = -(\gamma_{50}+\gamma_{51}+\gamma_{52}+\gamma_{53}+\gamma_{54}+2\frac{\sigma I_P(z,t)}{\hbar\omega_P}).$$

Once again, only the change of the spatial mean population is needed. By applying the spatial mean to (2.23), we get

$$\frac{\partial \bar{\mathbf{N}}}{\partial t} = \frac{1}{L}\int_0^L \mathbf{\Gamma}(z,t)\mathbf{N}(z,t)dz + \frac{1}{L}\int_0^L \mathbf{\Gamma}_{dop}dz\ N_{dop}. \tag{2.24}$$

The first integral has no algebraic solution and (2.24) cannot be reduced to include average populations only. By once again assuming that the population does not vary greatly across the spatial dimension, i.e. $\mathbf{N}(z,t) \approx \bar{\mathbf{N}}(t)$, we can simplify (2.24) to

$$\frac{\partial \bar{\mathbf{N}}}{\partial t} = \frac{1}{L}\int_0^L \mathbf{\Gamma}(z,t)dz\ \bar{\mathbf{N}}(t) + \frac{1}{L}\int_0^L \mathbf{\Gamma}_{dop}dz\ N_{dop}. \tag{2.25}$$
$$= \bar{\mathbf{\Gamma}}\bar{\mathbf{N}} + \bar{\mathbf{\Gamma}}_{dop}N_{dop}. \tag{2.26}$$

Inside the matrix $\mathbf{\Gamma}$ as well as the vector $\mathbf{\Gamma}_{dop}$ only the pump beam intensity I_P depends on the position and is linear in all their components. We can therefore get $\bar{\mathbf{\Gamma}}$ and $\bar{\mathbf{\Gamma}}_{dop}$ by replacing I_P by its spatial mean value $\bar{I}_P$, which can be calculated using

$$\bar{I}_P = \frac{\exp[\sigma_P(\begin{bmatrix}1 & 1 & 1 & 1 & 2\end{bmatrix}\bar{\mathbf{N}} - N_{dop})L] - 1}{\sigma_P(\begin{bmatrix}1 & 1 & 1 & 1 & 2\end{bmatrix}\bar{\mathbf{N}} - N_{dop})L} I_P(0,t), \tag{2.27}$$

yielding

$$\bar{\mathbf{\Gamma}} = \begin{bmatrix} \Gamma_{11} & (\gamma_{21}-\gamma_{01}) & -\gamma_{01} & -\gamma_{01} & \gamma_{51}-\gamma_{01} \\ \gamma_{21}-\gamma_{02} & \Gamma_{22} & \gamma_{32}-\gamma_{02} & -\gamma_{02} & \gamma_{52}-\gamma_{02} \\ -\gamma_{03} & \gamma_{23}-\gamma_{03} & \Gamma_{33} & \gamma_{43}-\gamma_{03} & \gamma_{53}-\gamma_{03} \\ -\gamma_{04} & -\gamma_{04} & \gamma_{34}-\gamma_{04} & \Gamma_{44} & -\gamma_{04} \\ -\frac{\sigma \bar{I}_P(t)}{\hbar\omega_P} & -\frac{\sigma \bar{I}_P(t)}{\hbar\omega_P} & -\frac{\sigma \bar{I}_P(t)}{\hbar\omega_P} & -\frac{\sigma \bar{I}_P(t)}{\hbar\omega_P} & \bar{\Gamma}_{55}(\bar{I}_P(t)) \end{bmatrix}, \bar{\mathbf{\Gamma}}_{dop} = \begin{bmatrix} \gamma_{01} \\ \gamma_{02} \\ \gamma_{03} \\ \gamma_{04} \\ \frac{\sigma \bar{I}_P(t)}{\hbar\omega_P} \end{bmatrix}$$

Assuring that the pump light intensity only changes slowly, enables us to set the pump intensity constant in between two pulses. The change in population during the pumping

process does not change the spatial mean of the pump intensity by much i.e. $\bar{I}_P(t) \approx \bar{I}_P(0)$. Equation (2.26) can then be solved using methods for linear differential matrix equations.

$$\bar{\mathbf{N}}(t) = \mathbf{exp}[\bar{\mathbf{\Gamma}}t]\bar{\mathbf{N}}(0) + \int_0^t \mathbf{exp}[\bar{\mathbf{\Gamma}}t']dt'\ \bar{\mathbf{\Gamma}}_{dop}N_{dop} \tag{2.28}$$

This equation can now be used to calculate the population change between two pulses by setting the time accordingly.

2.5 Assembling the reduced-order model

The operation of the regenerative amplifier can be split into three phases.

1. the pulse amplification inside the gain medium during a single passage
2. the pulse circulating back inside the resonator cavity
3. a regeneration phase after release of the last pulse until the next seed pulse is injected

In the first phase, we can use (2.10) and (2.17) to calculate the population change and use (2.12) to estimate the amplification of the pulse. These equations can be collected in two mappings, the vector functional

$$\mathbf{f}_N(\bar{\mathbf{N}}, \hat{E}_{in,RA}) = \bar{\mathbf{N}} + \begin{bmatrix} \frac{1}{2\hbar}\int_{-\infty}^{\infty} \frac{\exp\left[2\alpha_G(\omega,\bar{\mathbf{N}})L\right]-1}{2\alpha_G(\omega,\bar{\mathbf{N}})L}|\hat{E}_{in,RA}(\omega)|^2\mathrm{Im}\{\chi_1(\omega,\Delta\bar{N}_{51})\}d\omega, \\ \frac{1}{2\hbar}\int_{-\infty}^{\infty} \frac{\exp\left[2\alpha_G(\omega,\bar{\mathbf{N}})L\right]-1}{2\alpha_G(\omega,\bar{\mathbf{N}})L}|\hat{E}_{in,RA}(\omega)|^2\mathrm{Im}\{\chi_2(\omega,\Delta\bar{N}_{52})\}d\omega, \\ \frac{1}{2\hbar}\int_{-\infty}^{\infty} \frac{\exp\left[2\alpha_G(\omega,\bar{\mathbf{N}})L\right]-1}{2\alpha_G(\omega,\bar{\mathbf{N}})L}|\hat{E}_{in,RA}(\omega)|^2\mathrm{Im}\{\chi_3(\omega,\Delta\bar{N}_{53})\}d\omega, \\ \frac{1}{2\hbar}\int_{-\infty}^{\infty} \frac{\exp\left[2\alpha_G(\omega,\bar{\mathbf{N}})L\right]-1}{2\alpha_G(\omega,\bar{\mathbf{N}})L}|\hat{E}_{in,RA}(\omega)|^2\mathrm{Im}\{\chi_4(\omega,\Delta\bar{N}_{54})\}d\omega, \\ -\sum_{j=1}^{4}\frac{1}{2\hbar}\int_{-\infty}^{\infty} \frac{\exp\left[2\alpha_G(\omega,\bar{\mathbf{N}})L\right]-1}{2\alpha_G(\omega,\bar{\mathbf{N}})L}|\hat{E}_{in,RA}(\omega)|^2\mathrm{Im}\{\chi_j(\omega,\Delta\bar{N}_{5j})\}d\omega. \end{bmatrix} \tag{2.29a}$$

connecting initial and end populations, as well as the functional

$$f_E(\bar{\mathbf{N}}, \hat{E}_{in,RA}(\omega)) = \exp\left[-i\left(L\frac{k_2}{2}\omega^2 + \frac{\omega_0^2}{2c_0^2\varepsilon_0 k_0}\sum_{j=1}^{4}\chi_j(\omega,\Delta\bar{N}_{5j}^0)\right)\right]\hat{E}_{in,RA}(\omega), \tag{2.29b}$$

connecting the input and output pulses. These equations can be combined in the pulse model

$$\begin{bmatrix}\bar{\mathbf{N}}^{k,n+1} \\ \hat{E}_{out,RA}^{k,n}\end{bmatrix} = \begin{bmatrix}\mathbf{f}_N(\bar{\mathbf{N}}^{k,n}, \hat{E}_{in,RA}^{k,n}) \\ f_E(\bar{\mathbf{N}}^{k,n}, \hat{E}_{in,RA}^{k,n})\end{bmatrix}, \tag{2.30}$$

which describes the effect of a single passage of a pulse $\hat{E}_{in,RA}^{k,n}$ through the gain medium. One round trip is completed after the circulation of the pulse through the cavity, which

introduces the cavity losses η_{RC}, resulting in the inputs for the next round trip

$$\begin{bmatrix} \bar{\mathbf{N}}^{k,n+1} \\ \hat{E}^{k,n+1}_{in,RA} \end{bmatrix} = \begin{bmatrix} \mathbf{f}_N(\bar{\mathbf{N}}^{k,n}, \hat{E}^{k,n}_{in,RA}) \\ \eta_{RC} f_E(\bar{\mathbf{N}}^{k,n}, \hat{E}^{k,n}_{in,RA}) \end{bmatrix}. \tag{2.31}$$

$$= \mathbf{f}_{RT}\left(\begin{bmatrix} \bar{\mathbf{N}}^{k,n} \\ \hat{E}^{k,n}_{in,RA} \end{bmatrix} \right) \tag{2.32}$$

The second phase is a pumping and relaxation phase and can be described using (2.28) with a pump time t equal to the return time of the pulse circulating back through the cavity

$$\frac{L_{RC} - L}{c_0} \approx 13\text{ns}, \tag{2.33}$$

with the length of the resonator cavity L_{RC}, the length of the gain medium L and the speed of light c_0. Within such a short time, the effect of relaxation and pumping is minimal. We can therefore neglect the population change during this phase. The third phase is also a pumping and relaxation phase, which can be described with (2.28). The total time of this third phase

$$\frac{1}{f_{rep}} - N_{RT}\left(\frac{L_{RC} - L}{c_0} + \frac{L}{c}\right), \tag{2.34}$$

with the seed repetition rate f_{rep}, the speed of light c inside the medium and the number of round trips N_{RT}. We can mitigate some of the error caused by neglecting the effects of relaxation and pumping during the pulse propagation, see the derivations of Section 2.3, as well as during the second phase by extending the time of this third phase to include phases one and two as well. The full pumping time is therefore defined as

$$T_{pump} = \frac{1}{f_{rep}}. \tag{2.35}$$

This procedure is similar to applying operator splitting to the reference model. The resulting equation

$$\mathbf{f}_{pump}(\bar{\mathbf{N}}) = \mathbf{exp}[\bar{\mathbf{\Gamma}}\frac{1}{f_{rep}}]\bar{\mathbf{N}}(0) + \int_0^{\frac{1}{f_{rep}}} \mathbf{exp}[\bar{\mathbf{\Gamma}}\ t]dt\ \bar{\mathbf{\Gamma}}_{dop} N_{dop} \tag{2.36}$$

comprises the pump model.

We can now use the pulse and pump models to assemble the reduced-order model. A schematic overview of the model is shown in Figure 2.3.

1. The k-th pulse starts with an initial pulse generated by filtering the seed pulse $\hat{E}^{k,1}_{in,RA} = f^k(\omega)\hat{E}_{seed}$ at an initial population $\bar{\mathbf{N}}^{k,1} = \bar{\mathbf{N}}^k_{init}$.

2. Propagation through the gain medium is modeled using (2.29a), resulting in $\bar{\mathbf{N}}^{k,2}$ and $\hat{E}^{k,1}_{out,RA}$.

3. During the return trip the pulse is reduced by the cavity losses η_{RC} to get $\hat{E}^{k,2}_{in,RA} = \eta_{RC}\hat{E}^{k,1}_{out,RA}$.
4. The next propagation is run immediately with the initial population $\bar{\mathbf{N}}^{k,2}$ and an input pulse $\hat{E}^{k,2}_{in,RA}$, resulting in $\bar{\mathbf{N}}^{k,3}$ and $\hat{E}^{k,2}_{out,RA}$.
5. Steps 2 - 4 are repeated N_{RT} times.
6. The last output pulse $\hat{E}^{k,N_{RT}}_{out,RA}$ is then released from the cavity as the fully amplified pulse $\hat{E}^{k}_{out}$.
7. Now the last end population $\bar{\mathbf{N}}^{k,N_{RT}+1}$ is fed into the pump model (2.36) to get the initial population for the $(k+1)$-th pulse $\bar{\mathbf{N}}^{k+1}$.

Using the shorthand for function composition

$$f^N(x) = f \circ f \circ \cdots \circ f(x), \tag{2.37}$$

we can combine the functions (2.32) and (2.36) to get the next initial population

$$\bar{\mathbf{N}}^{k+1} = \mathbf{f}_{pump}\left(\begin{bmatrix}1 & 0\end{bmatrix}\mathbf{f}_{RT}^{N_{RT}}\left(\begin{bmatrix}\bar{\mathbf{N}}^{k} \\ \hat{E}^{k}_{in}(\omega)\end{bmatrix}\right)\right) = \mathbf{F}(\bar{\mathbf{N}}^{k}, \hat{E}^{k}_{in}(\omega)) \tag{2.38}$$

and the amplified pulse

$$\hat{E}^{k}_{out}(\omega) = \begin{bmatrix}0 & 1\end{bmatrix}\mathbf{f}_{RT}^{N_{RT}}\left(\begin{bmatrix}\bar{\mathbf{N}}^{k} \\ \hat{E}^{k}_{in}(\omega)\end{bmatrix}\right), \tag{2.39}$$

the equations above constitute a nonlinear discrete-time dynamic system in state-space form

$$\bar{\mathbf{N}}^{k+1} = \mathbf{F}(\bar{\mathbf{N}}^{k}, \hat{E}^{k}_{in}(\omega)), \quad \bar{\mathbf{N}}^{0} = \bar{\mathbf{N}}_{init} \tag{2.40a}$$

$$\hat{E}^{k}_{out}(\omega) = \mathrm{h}(\bar{\mathbf{N}}^{k}, \hat{E}^{k}_{in}(\omega)). \tag{2.40b}$$

2.6 Model comparison

In order to evaluate and visualize the validity of the reduced-order model, a single pulse was propagated through the reference model as well as the reduced-order model, starting from the same initial population. The number of round trips N_{RT} was set high enough to almost deplete the population inversion for all transitions. This is not a typical mode of operation, but is considered for illustrative purposes. Following the last round trip of the pulse, the pump model is run consecutively until a steady state is reached for all populations. Figure 2.4 shows the evolution of the different population inversions as well as the current energy of the circulating pulse

$$W^n = \frac{A_{beam}}{2Z_0}\int_{-\infty}^{\infty} |\hat{E}^{n}_{out,RA}(\omega)|^2 d\omega, \tag{2.41}$$

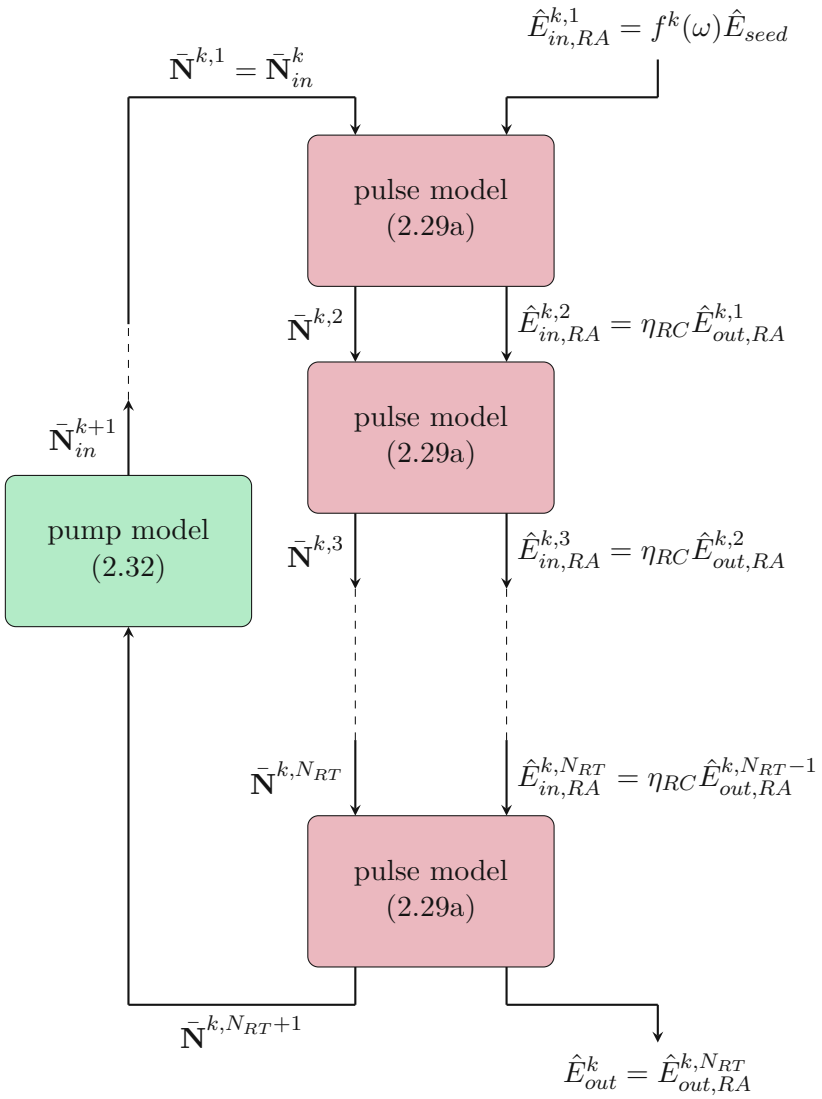

Figure 2.3: Coupling diagram of the reduced-order model.

with the beam area A_{beam} and the wave impedance Z_0. Because the dynamics of the pump model is significantly slower than the pulse model, a homogeneously scaled x-axis normalized to the total round-trip time

$$T_{RT} = \frac{L_{RC}}{c} = 13.5\text{ns} \tag{2.42}$$

is used.

These results show a good agreement of the mean population inversion $\Delta\bar{N}_{5j} = \bar{N}_5 - \bar{N}_j$ at highly saturated operation. This is true for both, the pulse propagation phase and the pumping phase. Mainly during the build-up phase of the pulse energy, significant deviations between the models are visible. These build-up phases, however, determine the pulse-to-pulse dynamics of the system.

We can also see here that the assumption about the difference in the dynamics between the pulse amplification and the pumping and relaxation is satisfied. The pump model needs a factor of 10^4 more time to regenerate the inversion than the pulse needed to deplete it, which confirms the assertion that the effect of pumping and relaxation during the amplification of the pulse is negligible.

2.7 Operating regions of regenerative amplifiers

The comparison in the previous section was concerned with the evolution of one laser pulse as well as the population inversion during the pumping phase afterwards. If this recovery is not sufficient to reach the initial inversion again, the amplification of the input pulse, as well as the change in population, are going to be different for the next pulse, as is described by the pulse-to-pulse dynamics (2.40). This dynamic can be split into three distinct regions.

1. Asymptotic and stable dynamics
2. Oscillating and stable dynamics
3. Unstable dynamics

An example of the first is plotted in Figure 2.5 using the reduced-order model. The asymptotic behavior is clearly visible in the output pulse energy, which monotonically approaches its steady-state value after around 12 pulses. An operation of the second type is plotted in Figure 2.6, again converging after around 12 pulses. The transient oscillation typical for the third type of operation is plotted in Figure 2.7. Due to the nonlinear behavior of the system, this unstable operation does not diverge to plus and minus infinity, instead it converges towards a limit cycle with a finite number of points.

Which of the three operation types is seen, mainly depends on four parameters:

1. The pump light intensity I_P: lower values generally tend to instability, because less inversion is build up between two pulses.
2. The frequency of the seed pulses f_{rep}: higher values tend to instability, because the shorter time between two pulses means less inversion is build up as well.

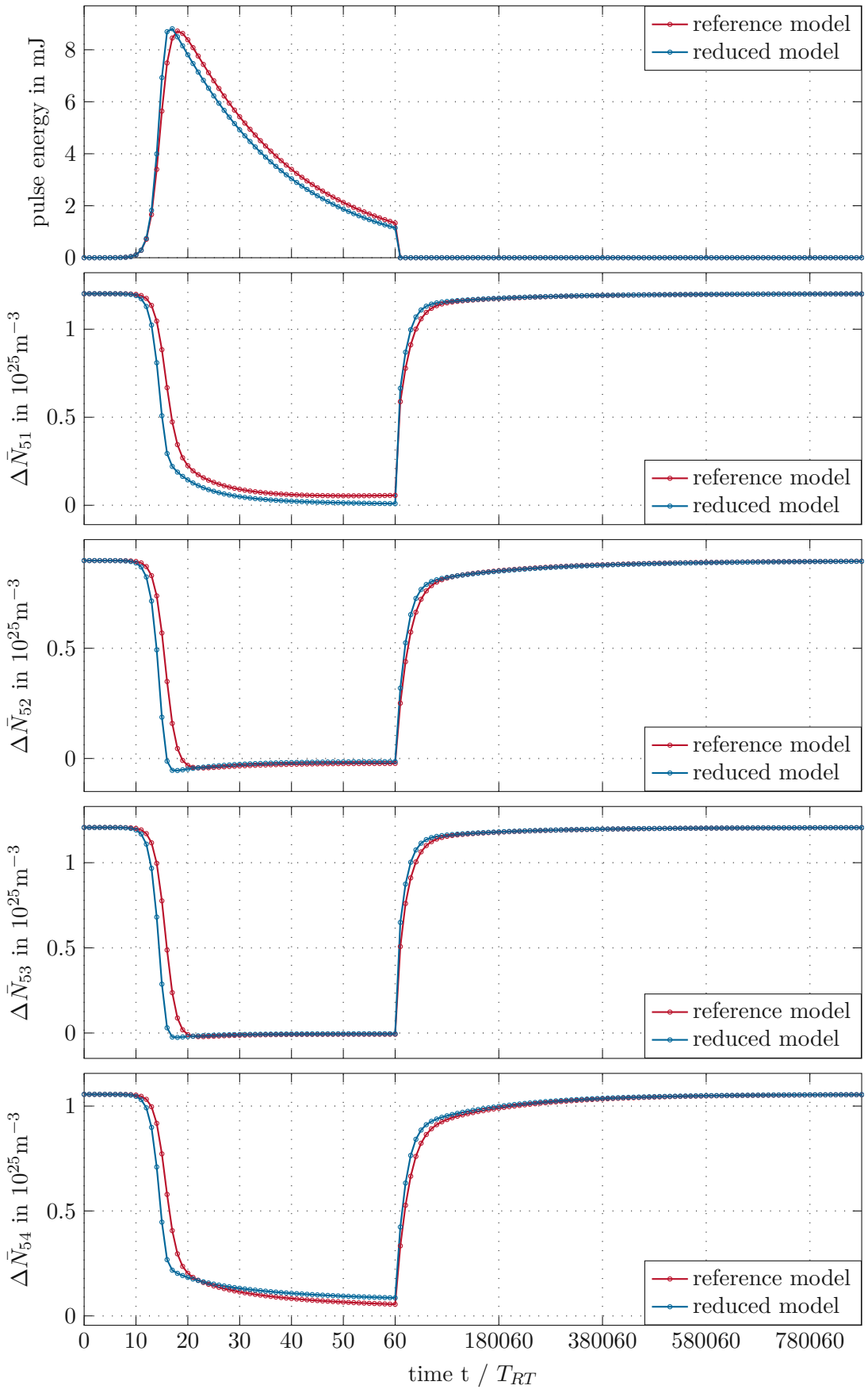

Figure 2.4: Reference model vs. reduced-order model: output energy and all population inversions.

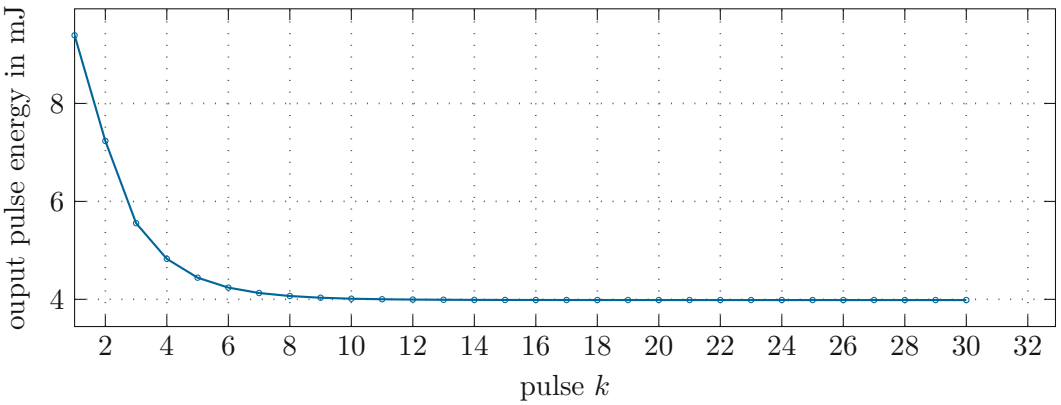

Figure 2.5: Pulse-to-pulse dynamics of the regenerative amplifier for an asymptotically stable operating point.

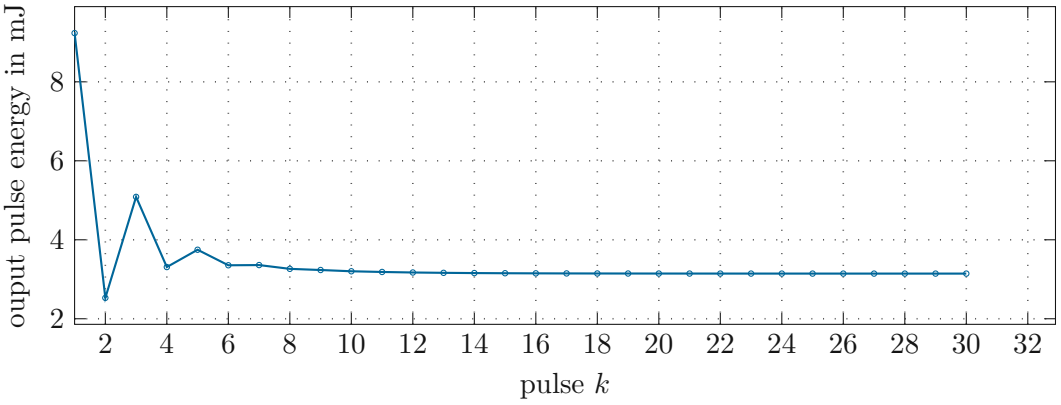

Figure 2.6: Pulse-to-pulse dynamics of the regenerative amplifier for an oscillating stable operating point.

3. The energy of the input pulse: lower energy generally tends to instability.
4. higher output pulse energies also lead to less stable behavior.
5. The number of round trips for each pulse N_{RT}: Round-trip numbers with high amplification generally also tend to more instability.

It is well known that this coupling of subsequent pulses can destabilize the amplifiers' dynamics and lead to period-doubling bifurcations and ultimately deterministic chaos [30][22].

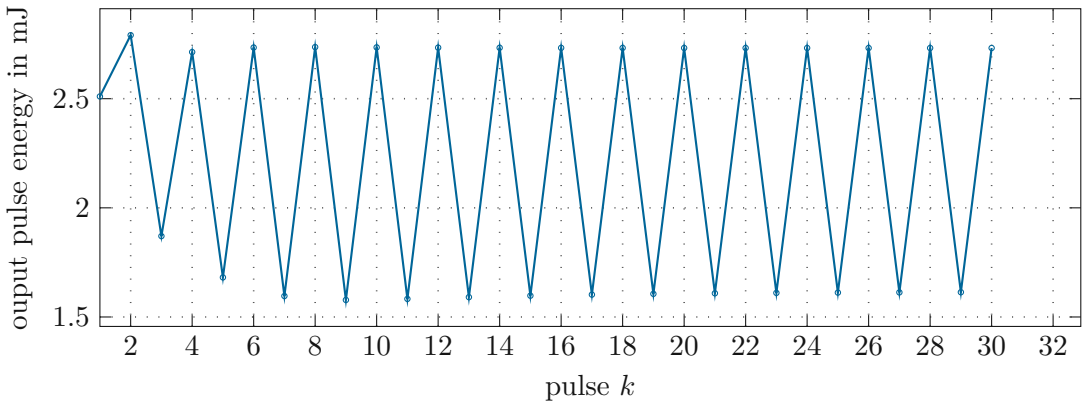

Figure 2.7: Pulse-to-pulse dynamics of the regenerative amplifier for an unstable operating point.

3 Parameter identification

Simplification steps to obtain the reduced-order model (2.40) necessarily entail errors, e.g., a slight overestimation of the actual gain by not considering depletion effects immediately. Such effects can be partly mitigated by adjusting selected parameter values of the reduced-order model. Moreover, most mathematical models have to be calibrated by measurements. This chapter thus aims to elucidate how well the reduced-order model can be fitted to the reference model and to measurement data. To facilitate this procedure the selection of viable parameters needs to be identified first. No implementation capable of online calibration for such a system has been explored previously, only one semi-automatic method was presented in [31].

3.1 Identifying viable parameters

A number of different parameters come into consideration for calibration. These parameters need to represent the interaction of the resonant transitions with the pulse as well as the dynamics of the pumping process. For the pulse interactions, the transition cross sections σ_j, $j = 1, \dots, 4$ are chosen as parameters. The pumping process is represented by the transition cross section σ_P of the pumping field as well as the relaxation probabilities γ_{i0}, $i = 1, \dots 5,$. Note here that the relaxation probabilities γ_{0i} are given by $\gamma_{0i} = BF_{0i}\gamma_{i0}$ using their respective Boltzmann factors

$$BF_{0i} = \exp\left(\frac{-E_i}{k_B T}\right). \tag{3.43}$$

In addition to this, the round-trip losses η_{RC} are also calibrated to represent the dissipative processes. Thus, the set of parameters $p_j \in \{\sigma_1, \sigma_2, \sigma_3, \sigma_4, \sigma_P, \eta_{RC}, \gamma_{01}, \gamma_{02}, \gamma_{03}, \gamma_{04}, \gamma_{05}\}$ is considered in the following.

To assess the viability of these parameters for calibration, the sensitivity of a set of values $y_i \in \{\bar{N}_1, \bar{N}_2, \bar{N}_3, \bar{N}_4, \bar{N}_5, W_{out}\}$ for a single step of the pulse-to-pulse dynamics (2.40) to changes of the parameters p_j is calculated using the sensitivity

$$S_{y_i,p_j} = \frac{\frac{\partial y_i}{\partial p_j}}{y_i}. \tag{3.44}$$

The output energy W_{out} is calculated by

$$W_{out} = \frac{A_{beam}}{2Z_0} \int_{-\infty}^{\infty} |\hat{E}^k_{out}(\omega)|^2 d\omega. \tag{3.45}$$

These output values are chosen because they represent the pulse-to-pulse dynamics, which are important for the controller design later on. The derivative is calculated using the

Table 3.1: Overview of the absolute value of the sensitivity $|S_{y_i,p_j}|$ in percent.

	σ_1	σ_2	σ_3	σ_4	σ_P	η_{RC}	γ_{01}	γ_{02}	γ_{03}	γ_{04}	γ_{05}
$\bar{N}_1$	0.297	0.132	0.14	0.157	4.435	0.11	0.196	7.11	0.096	5.083	0.89
$\bar{N}_2$	0.689	3.457	2.01	6.886	2.7	3.22	0.002	56.2	0.101	2.427	0.42
$\bar{N}_3$	0.312	0.147	0.15	0.182	3.463	0.11	0.002	7.05	11.77	5.074	0.69
$\bar{N}_4$	5.934	8.712	5.99	15.71	2.838	4.45	0.002	4.22	0.111	76.93	0.50
$\bar{N}_5$	0.358	0.194	0.18	0.26	3.871	0.10	0.002	6.85	0.096	5.032	0.82
W_{out}	20.46	21.36	27.9	8.487	0	237	0	0	0	0	0

complex step differentiation method, which is detailed in Section A.3. An overview of the sensitivity values is shown in Table 3.1.

The sensitivity values of each output to changes of the four transition cross sections σ_j are very similar. All the sensitivities of the pump light cross section σ_P are very similar, except for the $|S_{W_{out},\sigma_P}|$, which is zero because the pump model is only run after the amplification is finished as seen in (2.40). For the round-trip losses η_{RC}, we have very different sensitivities. The high sensitivity of $|S_{W_{out},\eta_{RC}}|$ is expected because the round-trip losses directly impact the pulse energy every round trip. We can see very different sensitivities for the relaxation probabilities, with the highest values of S being much lower for γ_{01} and γ_{05} when compared to the other three relaxation probabilities. Once again we can see the zero sensitivity of the pulse energy, which is due to the pump model only being executed after the amplification as well. Based on these observations all transition cross sections σ and the path losses η_{RC} are used as calibration parameters,

$$p_j \in \{\sigma_1, \sigma_2, \sigma_3, \sigma_4, \sigma_P, \eta_{RC}\}. \tag{3.46}$$

While the relaxation probabilities γ_{02}, γ_{03} and γ_{04} could be added as well, we note here that this only marginally improves the results.

3.2 Calibration with simulation data

This calibration scenario is designed to test how much the error between the two models can be reduced if we have access to all populations and energies during one pulse propagation due to (2.40). Such an approach is only possible because the data are generated by the reference model. This data is taken from the comparison simulation scenario of Figure 2.4 in the previous chapter.

The calibrated parameters $\mathbf{p}^*$ are calculated by solving the optimization problem

$$\mathbf{p}^* = \arg\min_{\mathbf{p}} \; J(\mathbf{p}). \tag{3.47}$$

The cost function $J(\mathbf{p})$ is assembled using the simulation data of the reference model. Setting $k = 1$, this data can be split into the populations $\bar{\mathbf{N}}_{ref}^{1,n}$ during the pulse amplification, the corresponding pulse energies

$$W_{ref}^{1,n} = \frac{A_{beam}}{2Z_0} \int_{-\infty}^{\infty} |\hat{E}_{out,RA}^{1,n}|^2 d\omega \tag{3.48}$$

and the populations $\bar{\mathbf{N}}^{k,n}_{pump,ref}$ during the recovery phase, which can be seen in Figure **??** for $\frac{t}{T_{RT}} \geq 60$, of which N_{RT} are taken equally spaced in time. Using the squared error in the cost function yields

$$J(\mathbf{p}) = \sum_{j=1}^{N_{RT}} [(|W^{1,j}(\mathbf{p}) - W^{1,j}_{ref}| \frac{1}{W_{Norm}})^2 + \|\bar{\mathbf{N}}^{1,j}(\mathbf{p}) - \bar{\mathbf{N}}^{1,j}_{ref}\|_2 \frac{1}{N_{Norm}})^2] \tag{3.49}$$

$$+ \sum_{j=1}^{N_{RT}} (\|\bar{\mathbf{N}}^{1,j}_{pump}(\mathbf{p}) - \bar{\mathbf{N}}^{1,j}_{pump,ref}\|_2 \frac{1}{N_{Norm}})^2 \tag{3.50}$$

with the scaling factors W_{Norm} and N_{Norm}. The optimization is solved using a trust-region type solver build into the *lsqnonlin* function provided by the Matlab Optimization Toolbox. Because all parameters are in very different value regions, the calibration results are going to be presented as multiplicative factors $\tilde{p}_j$ of the parameters used in the reference model $p_j = p_{j,ref}\tilde{p}_j$.

Table 3.2: Calibration results from full propagation information

	N_{Norm}	W_{Norm}	$\tilde{p}_1$ (σ_1)	$\tilde{p}_2$ (σ_2)	$\tilde{p}_3$ (σ_3)	$\tilde{p}_4$ (σ_4)	$\tilde{p}_5$ (σ_P)	$\tilde{p}_6$ (η_{RC})
V1	1.3592e25	0.0105	0.8213	0.8861	0.9875	0.9719	0.7636	0.9454
V2	1.3592e25	2.095e-4	1.0851	0.6203	1.0638	1.1807	0.7932	0.9468

This optimization was run with two different sets of scaling parameters. The resulting scaling factors for the parameters $\tilde{p}_j$ as well as the scaling in the cost function N_{Norm} and W_{Norm} are shown in Table 3.2. For these results, the relative energy error

$$e_W = \frac{W^{k,n} - W^{k,n}_{ref}}{W_{Norm,1}} \tag{3.51}$$

and the population inversion error between the calibrated and reference models are plotted in Figure 3.1. Both versions reduce the error of the pulse energy in the saturated operation and also reduce the error during the pumping process. The main difference between the two versions lies in how much the pulse energy error and the population inversion error are reduced during the regions with higher energy gain. Version 1 reduces the error of the population inversion further, but has increased pulse energy error in these high energy gain phases. Version 2 works opposite to that, by reducing the pulse energy error while not reducing the population inversion error as much as version 1 does. This behavior is as expected based on the higher cost of the pulse energy error in $J(\mathbf{p})$ of version 2. Adding in three relaxation probabilities γ_{02}, γ_{03} and γ_{04} as calibration parameters only marginally decreases the model error. The calibration using simulated data of a full propagation is clearly able to achieve better matching of the reduced-order and the reference model. We can also see the importance of scaling parameters on the quality of the results.

3.3 Calibration with steady-state measurements

Even though the calibration shown in the previous section is capable of reducing the error between the models in simulation, its usefulness in real-life application is very limited due

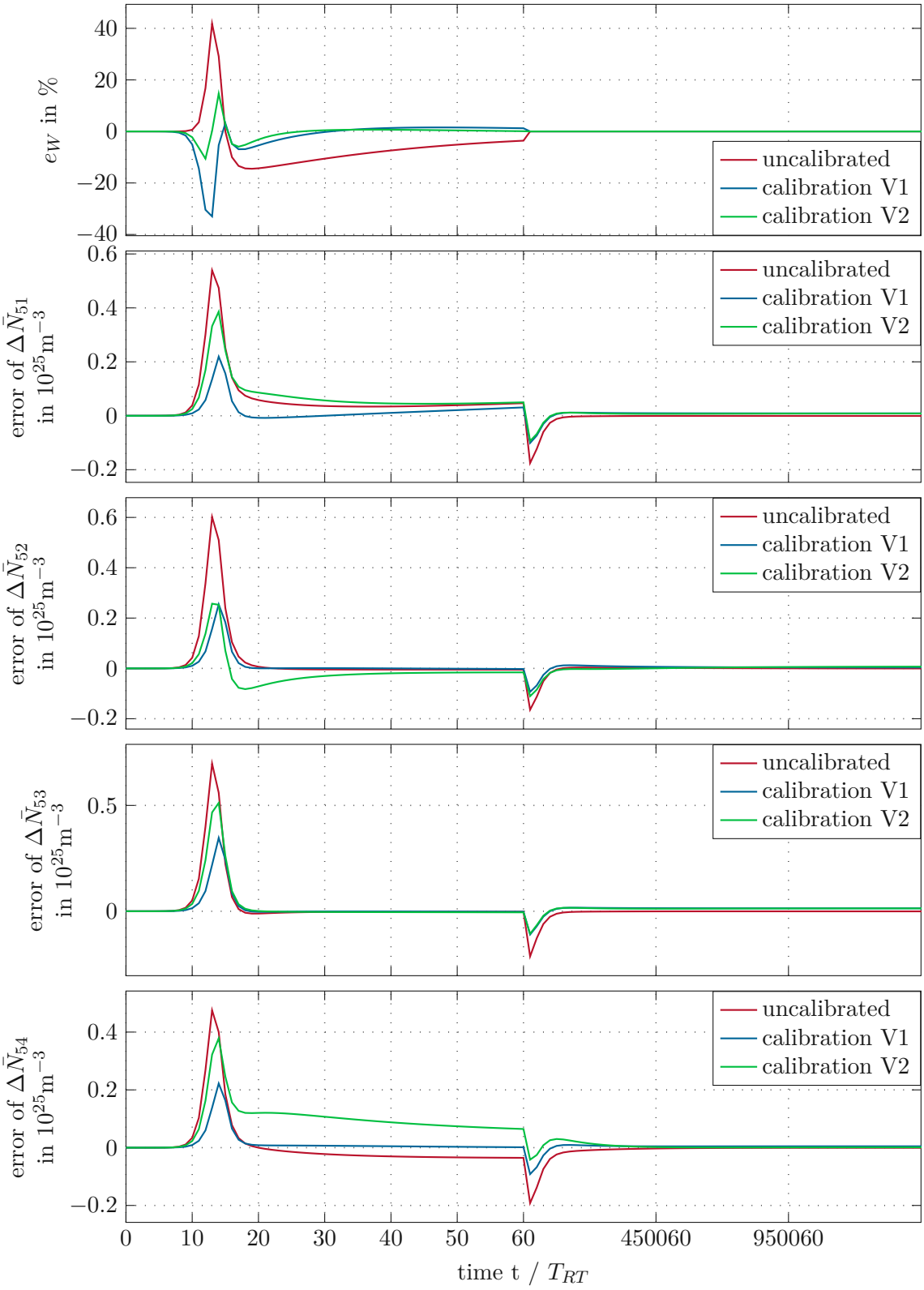

Figure 3.1: Comparison of the model error for the uncalibrated model and different calibration versions based on simulated data of the reference model. W_{norm} is set to be half of the maximum output energy.

to the lack of population measurements. Therefore, an alternate calibration regime using achievable measurements is introduced in this section. For a regenerative amplifier at 1 to 10 kHz, the system rapidly enters a steady-state regime for stable operating points, for which the pulse energy can be measured. These measurements are limited to stable operating points because the bifurcation of unstable operating points leads to a mean value being measured, which in general does not correspond to the corresponding steady-state value. To generate steady-state measurement data for this section, forward simulation of the reference model are used.

For the discrete-time system (2.40), we can calculate the steady-state mean populations $\bar{\mathbf{N}}^{ss}$ of the reduced-order model for a known input pulse $\hat{E}_{in}^{ss}(\omega)$ by solving

$$\bar{\mathbf{N}}^{ss} - \mathbf{F}(\bar{\mathbf{N}}^{ss}, \hat{E}_{in}^{ss}(\omega)) = \mathbf{0}. \tag{3.52}$$

The corresponding steady-state output pulse can then be calculated as

$$\hat{E}_{out}^{ss}(\omega) = \mathrm{h}(\bar{\mathbf{N}}^{ss}, \hat{E}_{in}^{ss}(\omega)). \tag{3.53}$$

To solve (3.52), different algorithms can be used. In this work *fsolve* from the Matlab Optimization Toolbox was employed.

Using only one steady-state measurements is clearly not sufficient because we want to optimize 6 parameters. Therefore, we want to use multiple different steady states, which can be generated by using different input pulses and pump intensities. Only using measurement of the full output pulse energy for the steady states of the reference model is problematic for the optimization algorithm used. The pulse energy is influenced by the cross sections σ_j of all transitions in a similar fashion, which leads to poor convergence of the optimization. To counteract this problem, spectrally resolved measurements are needed. They enable us to split the output pulse energy into multiple different partial energies, which correspond to specific spectral regions of the output pulse. Since the four transitions mainly amplify in their respective spectral regions, changes in one of these partial energies can be associated to the calibration parameters in different ways. Using the electric susceptibilities $\chi_j(\omega)$ for this splitting is practical because they correspond to the amplification by the different resonant transitions. Scaling them to have a maximum value of one yields the scaled susceptibilities $\tilde{\chi}_j(\omega)$ plotted in Figure 3.2. To calculate the split energies, the scaled susceptibilities are multiplied with the absolute squared output pulse and integrated, yielding

$$W_j^{ss} = \int_{-\infty}^{\infty} |\hat{E}_{out}^{ss}(\omega)|^2 \tilde{\chi}_j(\omega) d\omega, \quad j = 1, \ldots, 4. \tag{3.54}$$

For N_W input pulses and N_P pump intensities, the optimization problem

$$\mathbf{p}^* = \arg\min_{\mathbf{p}} \; J(\mathbf{p}), \tag{3.55}$$

with

$$J(\mathbf{p}) = \sum_{i=1}^{N_W} \sum_{l=1}^{N_P} \sum_{j=1}^{4} \left(\frac{W_j^{ss}(\mathbf{p}, W_{in,i}, I_{P,l}) - W_{j,ref}^{ss}(W_{in,i}, I_{P,l})}{E_{j,ref}^{ss}(W_{in,i}, I_{P,l})} \right)^2, \tag{3.56}$$

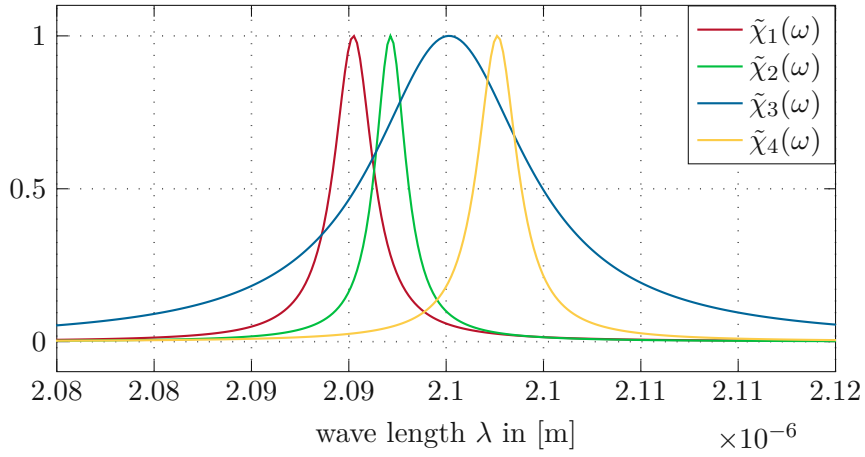

Figure 3.2: The scaled susceptibility functions used in the energy splitting needed for calibration.

must be solved, which is again done using the *Matlab* function *lsqnonlin*. The different input energies $W_{in,i}$ are achieved by scaling the input pulse

$$\hat{E}_{in,i}(\omega) = \hat{E}_{in,norm}(\omega)\sqrt{\frac{W_{in,i}}{W_{in,norm}}}, \tag{3.57}$$

The calibration parameters obtained by solving (3.55) are presented in Table 3.3. For a detailed breakdown of the calibrations results for different input energy and pump intensity selections, as well as the comparison criteria, see Section A.4.

Table 3.3: Chosen calibration results from steady-state measurements.

$\tilde{p}_1$ (σ_1)	$\tilde{p}_2$ (σ_2)	$\tilde{p}_3$ (σ_3)	$\tilde{p}_4$ (σ_4)	$\tilde{p}_5$ (σ_P)	$\tilde{p}_6$ (η_{RC})
0.9377	0.9692	0.9880	1.0037	1.0701	1.0901

Overall we can see that most of the scaling factors do differ significantly from the calibration in the previous section. The same scenario as previously, but simulated with the new calibrated parameters, is plotted in Figure 3.3 for comparison. The quality of the calibration based on steady-state measurements in most cases is worse than using the simulated data, especially the pulse energy for high round-trip values, which is expected because the steady-state measurements used for calibration are all gathered at $N_{RT} = 21$. The reproduction of the population inversions is better using the steady-state measurements even though they are not directly weighted in the cost function. This is likely due to the population dynamics dictating the steady-state populations and thus the steady-state output energies W_{out}^{ss}. Since the pulse-to-pulse dynamics of the model is of interest, an example of a stable operation is plotted in Figure 3.4 and of an unstable operation in Figure 3.5. Starting with the same initial mean population, all three models converge to a steady state, with a stationary difference remaining. The calibrated model shows less divergence from the reference model, with the pulse energy

showing the lowest error just as expected, except for $\Delta\bar{N}_{54}$ for which the uncalibrated model matches quite good already. Overall the presented steady-state calibration using spectral output measurements appears to be a valid strategy. It is important to note here that the spatially averaged populations of the reference model are calculated ex post and do not necessarily have to be reproduced by the reduced-order model, which is calibrated to the input-output behavior.

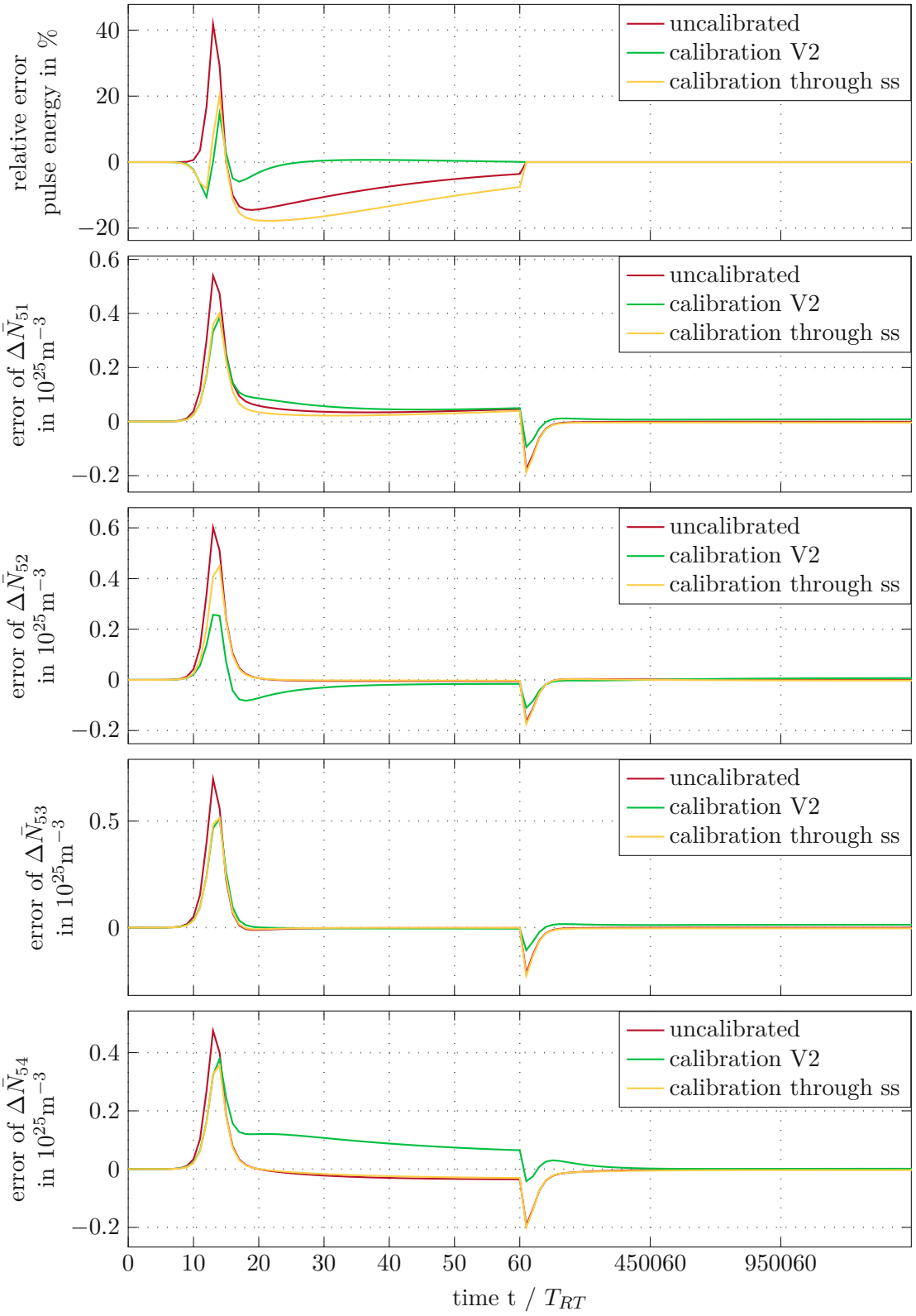

Figure 3.3: Comparison of the model errors of the uncalibrated and two calibrated models, one using the whole propagation and one using steady-state measurements of the reference model. The same propagation as in Figure 2.4 and Figure 3.1 is used.

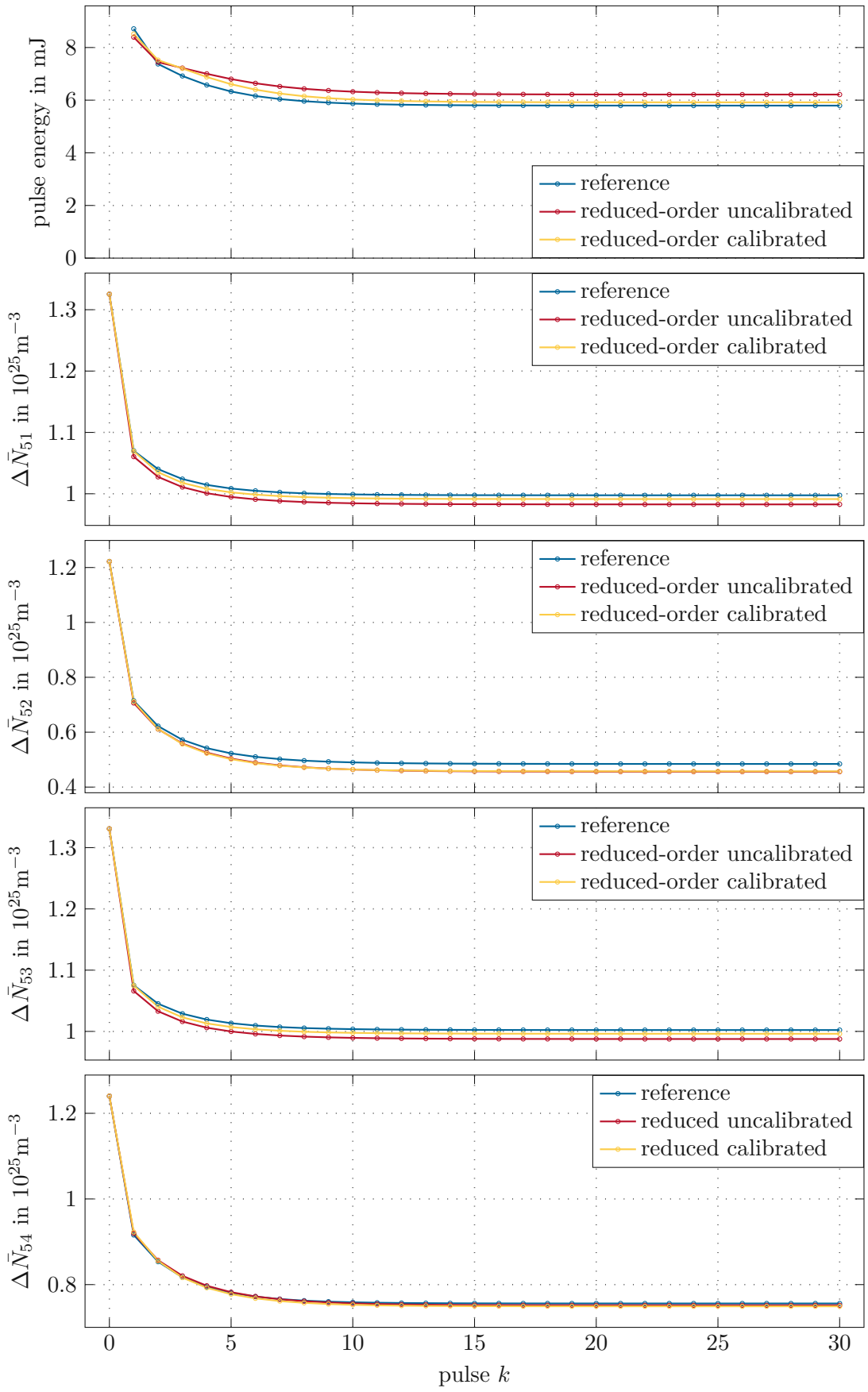

Figure 3.4: Pulse-to-pulse dynamics of a stable operating point of the reference model compared to the uncalibrated and calibrated reduced-order models.

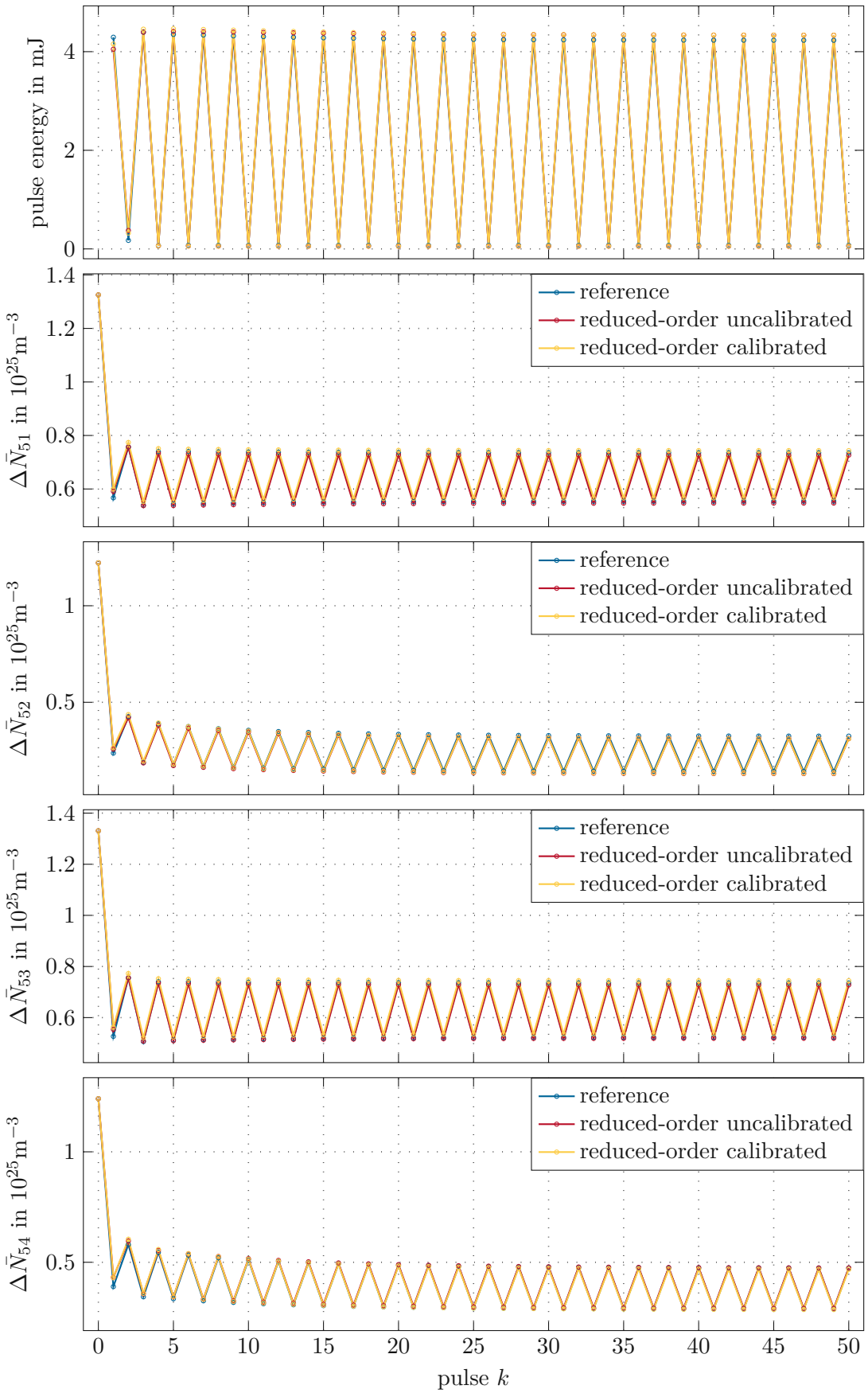

Figure 3.5: Pulse-to-pulse dynamics of an unstable operating point of the reference model compared to the uncalibrated and calibrated reduced-order models.

4 Stabilization of unstable operating points

As shown in Section 2.7, the regenerative amplifier can enter unstable operating points that result in period-doubling bifurcation. To suppress these bifurcations, a stabilizing state feedback controller, using the Linear Quadratic Regulator (LQR) method, combined with an Extended Kalman Filter (EKF) state estimator, is designed in this chapter.

4.1 State feedback controller design

This feedback control algorithm shall use measurements of the output pulse energy W_{out}^k to modify the pulse-to-pulse dynamics using $\hat{E}_{in}^k(\omega)$. The input pulse $\hat{E}_{in}^k(\omega)$ can be freely adjusted via the optical filter $f^k(\omega)$, except for limitations due to the passive nature of $f^k(\omega)$, i.e., $|f^k(\omega)| \leq 1$ or equally $|\hat{E}_{in}^k(\omega)| \leq |\hat{E}_{seed}(\omega)|$. See Figure 4.1 for a graphical representation of $\hat{E}_{seed}(\omega)$. The resulting input pulse $\hat{E}_{in}^k(\omega)$ for a desired input pulse $\hat{E}_{in}^{k,des}(\omega)$ can be defined as

$$\hat{E}_{in}^k(\omega) = \begin{cases} \hat{E}_{in}^{k,des}(\omega) & |\hat{E}_{in}^{k,des}(\omega)| \leq |\hat{E}_{seed}^k(\omega)| \\ \hat{E}_{seed}^k(\omega) & else. \end{cases} \tag{4.58}$$

Alternatively this can be written by defining the input filter

$$f^k(\omega) = \begin{cases} 1\exp\left[i(\phi(\hat{E}_{in}^{k,des}(\omega)) - \phi(\hat{E}_{seed}^k(\omega))\right] & \frac{|\hat{E}_{in}^{k,des}(\omega)|}{|\hat{E}_{seed}^k(\omega)|} \geq 1 \\ \frac{\hat{E}_{in}^{k,des}(\omega)}{\hat{E}_{seed}^k(\omega)} & else, \end{cases} \tag{4.59}$$

with $\phi(\hat{E})$ denoting the phase of $\hat{E}$.

This adjustment influences the shape and energy of the input pulse. Since the population dynamics are mainly driven by the input pulse energy, we choose to modify the energy of $\hat{E}_{in}^k(\omega)$ with the controller while keeping the shape fixed, i.e.

$$\hat{E}_{in}^k(\omega) = \hat{E}_{in}^{ss}(\omega)\sqrt{1 + u_{FB}^k}, \tag{4.60}$$

for the input energy this means that

$$W_{in}^k = W_{in}^{ss}(1 + u_{FB}^k), \tag{4.61}$$

with the input energy scaling parameter u_{FB}. The steady-state input pulse $\hat{E}_{in}^{ss}(\omega)$ can be chosen arbitrarily, which is used in the following chapter to shape the output pulse. A particularly easy input pulse choice is a scaled version of the seed pulse $\hat{E}_{seed}(\omega)$, e.g.

$$\hat{E}_{in}^{ss}(\omega) = \frac{1}{\sqrt{2}}\hat{E}_{seed}(\omega) \tag{4.62}$$

with the resulting input pulse

$$\hat{E}_{in}^{k}(\omega) = \frac{1}{\sqrt{2}}\hat{E}_{seed}(\omega)\sqrt{1+u_{FB}}, \qquad \text{for} \qquad u_{FB} \in (-1;1]. \tag{4.63}$$

This can be achieved using a simple gray-scale optical filter. Since the energy of a pulse scales with the squared electric field strength this results in $u_{FB}^{k} = 1$ corresponding to $\hat{E}_{in}^{k}(\omega) = \sqrt{2}\hat{E}_{in}^{ss}(\omega) = \hat{E}_{seed}(\omega)$. Note here that the upper limit of u_{FB}^{k} changes with shape of the input pulse. The discrete-time system in (2.40) can be reshaped for this new input pulse and using the easily measurable total output energy W_{out}^{k}, which can be calculated using (2.41), to get the discrete-time system for feedback control

$$\bar{\mathbf{N}}^{k+1} = \mathbf{F}\Big(\bar{\mathbf{N}}^{k}, \hat{E}_{in}^{ss}(\omega)\sqrt{1+u_{FB}^{k}}\Big), \tag{4.64a}$$

$$W_{out}^{k} = \mathrm{h}_{meas}\Big(\bar{\mathbf{N}}^{k}, \hat{E}_{in}^{ss}(\omega)\sqrt{1+u_{FB}^{k}}\Big) = \frac{A_{beam}}{2Z_0}\int_{-\infty}^{\infty}\Big|\mathrm{h}\Big(\bar{\mathbf{N}}^{k}, \hat{E}_{in}^{ss}(\omega)\sqrt{1+u_{FB}^{k}}\Big)\Big|^{2}d\omega. \tag{4.64b}$$

The first step in designing the state feedback controller is linearizing the dynamics in (4.66) around the steady state

$$\bar{\mathbf{N}}^{ss} = \mathbf{F}(\bar{\mathbf{N}}^{ss}, \hat{E}_{in}^{ss}(\omega)), \tag{4.65}$$

yielding

$$\Delta\bar{\mathbf{N}}^{k+1} = \mathbf{\Phi}\Delta\bar{\mathbf{N}}^{k} + \mathbf{\Gamma}u_{FB}^{k}, \tag{4.66a}$$

$$\Delta W_{out}^{k} = \mathbf{C}\Delta\bar{\mathbf{N}}^{k} + du_{FB}^{k}, \tag{4.66b}$$

with

$$\mathbf{\Phi} = \frac{\partial\mathbf{F}}{\partial\bar{\mathbf{N}}^{k}}(\bar{\mathbf{N}}^{k}, \hat{E}_{in}^{ss}(\omega)), \quad \mathbf{\Gamma} = \frac{\partial\mathbf{F}}{\partial u_{FB}^{k}}(\bar{\mathbf{N}}^{k}, \hat{E}_{in}^{ss}(\omega)), \tag{4.66c}$$

$$\mathbf{C} = \frac{\partial h_{meas}}{\partial\bar{\mathbf{N}}^{k}}(\bar{\mathbf{N}}^{k}, \hat{E}_{in}^{ss}(\omega)), \quad d = \frac{\partial h_{meas}}{\partial u_{FB}^{k}}(\bar{\mathbf{N}}^{k}, \hat{E}_{in}^{ss}(\omega)), \tag{4.66d}$$

and the linearized state $\Delta\bar{\mathbf{N}}^{k} = \bar{\mathbf{N}}^{k} - \bar{\mathbf{N}}^{ss}$ and output energy $\Delta W_{out}^{k} = W_{out}^{k} - h_{meas}(\bar{\mathbf{N}}^{ss}, \hat{E}_{in}^{ss}(\omega))$. This linearization is once again calculated using the complex step differentiation method in Section A.3. The controllability and observability of the linearized system (4.66) can always be shown for steady states where coupling between consecutive pulses is present. We now want to design a linear feedback control law

$$u_{FB}^{k} = \mathbf{K}_{FB}\Delta\bar{\mathbf{N}}^{k}, \tag{4.67}$$

using the control gain matrix $\mathbf{K}_{FB}$. One simple method to calculate $\mathbf{K}_{FB}$ is pole placement, where it is calculated such that the eigenvalues of the closed-loop system are placed at specific values. A problem with this method is the choice of the desired eigenvalues and high values of u_{FB} if these eigenvalues are chosen poorly. To circumvent this problem, the Linear Quadratic Regulator (LQR) method is used. This feedback controller design

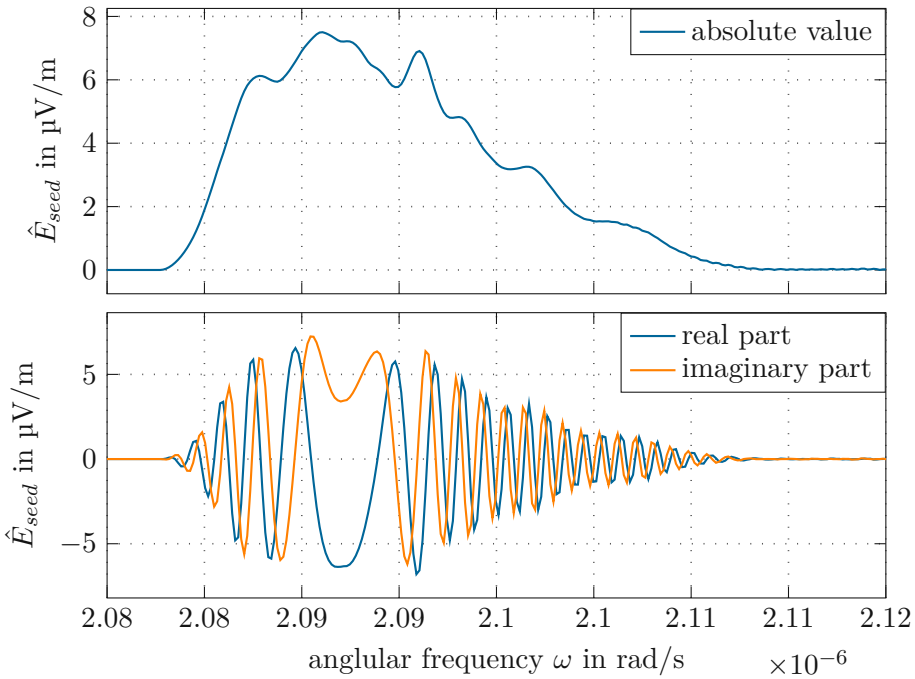

Figure 4.1: Seed pulse $\hat{E}^k_{seed}$ which is filtered to be used as the input pulse $\hat{E}^k_{in}$ of the regenerative amplifier.

method calculates a time-dependent $\mathbf{K}^k_{FB}$ such that the resulting series of $\bar{N}^k$ and u^k_{FB} minimizes the cost function

$$J(\bar{\mathbf{N}}^0) = \sum_{k=0}^{N-1} ((\Delta\bar{\mathbf{N}}^k)^T \mathbf{Q} \Delta\bar{\mathbf{N}}^k + R(u^k_{FB})^2 + 2u^k_{FB}\mathbf{S}\Delta\bar{\mathbf{N}}^k), \tag{4.68}$$

with the weighting matrix for the states $\mathbf{Q}$, the weighting vector for the product of state and input $\mathbf{S}$ and the weighting factor R for the input. Which must be chosen such that

$$\begin{bmatrix} Q & S \\ S^T & R \end{bmatrix} \tag{4.69}$$

is positive definite. A constant $\mathbf{K}_{FB}$ can be obtained by calculating the solution of (4.68) for $N \to \infty$. This desired feedback gain can be computed by solving the discrete Riccati-Equation

$$\mathbf{P}_s = (\mathbf{Q} + \mathbf{\Phi}^T \mathbf{P}_s \mathbf{\Phi}) - (\mathbf{S} + \mathbf{\Gamma}^T \mathbf{P}_s \mathbf{\Phi})^T (R + \mathbf{\Gamma} \mathbf{P}_s \mathbf{\Gamma})^{-1} (\mathbf{S} + \mathbf{\Gamma}^T \mathbf{P}_s \mathbf{\Phi}) \tag{4.70a}$$

for $\mathbf{P}_s$ and calculating

$$\mathbf{K}_{FB} = -(R + \mathbf{\Gamma} \mathbf{P}_s \mathbf{\Gamma})^{-1} (\mathbf{S} + \mathbf{\Gamma}^T \mathbf{P}_s \mathbf{\Phi}). \tag{4.70b}$$

For a detailed breakdown of the derivations for this controller design, see, e.g. [32]. Using this feedback law results in the closed-loop dynamics

$$\bar{\mathbf{N}}^{k+1} = \mathbf{F}\Big(\bar{\mathbf{N}}^k, \hat{E}^{ss}_{in}(\omega)\sqrt{1 + \mathbf{K}_{FB}\Delta\bar{\mathbf{N}}^k}\Big), \tag{4.71}$$

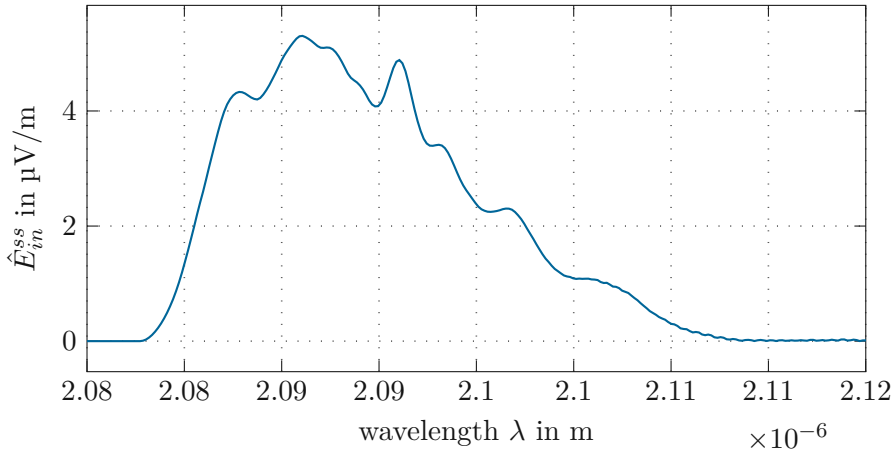

Figure 4.2: Experimental input pulse $\hat{E}_{in}^{ss}(\omega) = \frac{1}{\sqrt{2}}\hat{E}_{seed}(\omega)$ used for testing the stabilization of an unstable operating point.

with the linearized dynamic matrix of the closed loop system

$$\mathbf{\Phi}_{cl} = \mathbf{\Phi} + \mathbf{\Gamma}\mathbf{K}_{FB}. \tag{4.72}$$

If all eigenvalues of $\mathbf{\Phi}_{cl}$ lie within the unit circle, the closed-loop system is stable in a local region around the steady state $\bar{\mathbf{N}}^{ss}$ for $u_{FB} = 0$.

The main parameters of the uncontrolled system are the seed pulse frequency f_{rep}, the seed pulse energy W_{in} as well as its spectral shape, the pump intensity I_P, and the number of round trips N_{RT}, as discussed in Section 2.7. For example using the input pulse in Figure 4.2, which has a seed energy of 2.7 µJ, with a pump intensity of 119.37 W/mm^2, at a seed pulse frequency of 10 kHz and a round-trip number of 35, results in an unstable operating point. The eigenvalues of the open-loop dynamic matrix $\mathbf{\Phi}$ are plotted in Figure 4.3, together with the eigenvalues of the closed-loop dynamic matrix $\mathbf{\Phi}_{cl}$, for $\mathbf{Q} = \mathbf{I}$, $\mathbf{S} = \mathbf{0}$ and $R = 1$.

The evolution of the output energy as well as the population inversion for a stabilized amplifier using the feedback law (4.67) with (4.70) is shown in Figure 4.4 with the corresponding steady-state of the reduced-order model. The system is simulated for 15 pulses before the plotted values, so that the limit cycle is fully emerged. Then the controller is activated after the 10th plotted pulse, which enables to dampen the limit-cycle oscillations to a steady-state. The controller clearly accomplishes the goal of stabilizing the system. Also apparent is the constant population and output energy error that remains, which also means that u_{FB} reaches a nonzero steady state. This is a result of the error between the reference and reduced-order models, which brings along that the mean population of the reference model's steady state is different from the steady-state population of the reduced-order model. This is in principle not a problem for the application in this thesis, since subsequent pulse shaping methods only require the system to be stable, but it may limit the available control range of the optical filter, as can be seen in Figure 4.4.

In order to force the system to reach a steady state with $u_{FB}^{ss} = 0$, the system is extended

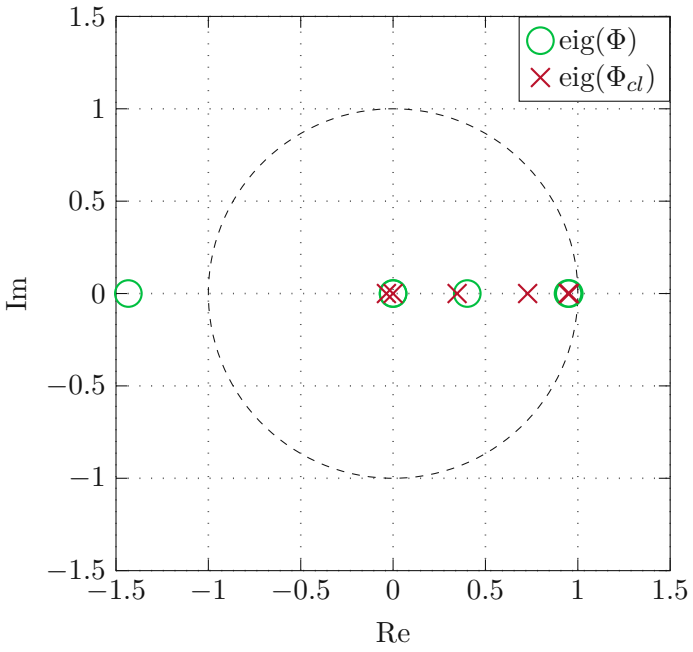

Figure 4.3: Eigenvalues of the dynamic matrix for the open-loop and closed-loop system.

by a differentiator directly in front of the control input u_{FB}. This implementation can also mitigate problems originating from an output energy error of the reduced-order model's steady-state compared to the reference model. By introducing an additional state z^k, which follows the discrete dynamics

$$z^{k+1} = r^k \tag{4.73}$$

with the new input r^k and defining

$$u_{FB}^k = z^{k+1} - z^k = r^k - z^k, \tag{4.74}$$

the extended system can be written as

$$\begin{bmatrix} \bar{\mathbf{N}}^{k+1} \\ z^{k+1} \end{bmatrix} = \mathbf{F}_e(\bar{\mathbf{N}}^k, z^k, r^k) = \begin{bmatrix} \mathbf{F}\left(\bar{\mathbf{N}}^k, \hat{E}_{in}^{ss}(\omega)\sqrt{1 + r^k - z^k}\right) \\ r^k \end{bmatrix}. \tag{4.75}$$

This extended system also again be stabilized by means of a LQR. Using the linearized model of the extended system

$$\begin{bmatrix} \Delta\bar{\mathbf{N}}^{k+1} \\ z^{k+1} \end{bmatrix} = \mathbf{\Phi}_e \begin{bmatrix} \Delta\bar{\mathbf{N}}^k \\ z^k \end{bmatrix} + \mathbf{\Gamma}_e r^k, \tag{4.76}$$

with the matrices

$$\mathbf{\Phi}_e = \begin{bmatrix} \mathbf{\Phi} & -\mathbf{\Gamma} \\ \mathbf{0} & 0 \end{bmatrix} \quad \text{and} \quad \mathbf{\Gamma}_e = \begin{bmatrix} \mathbf{\Gamma} \\ 1 \end{bmatrix}, \tag{4.77}$$

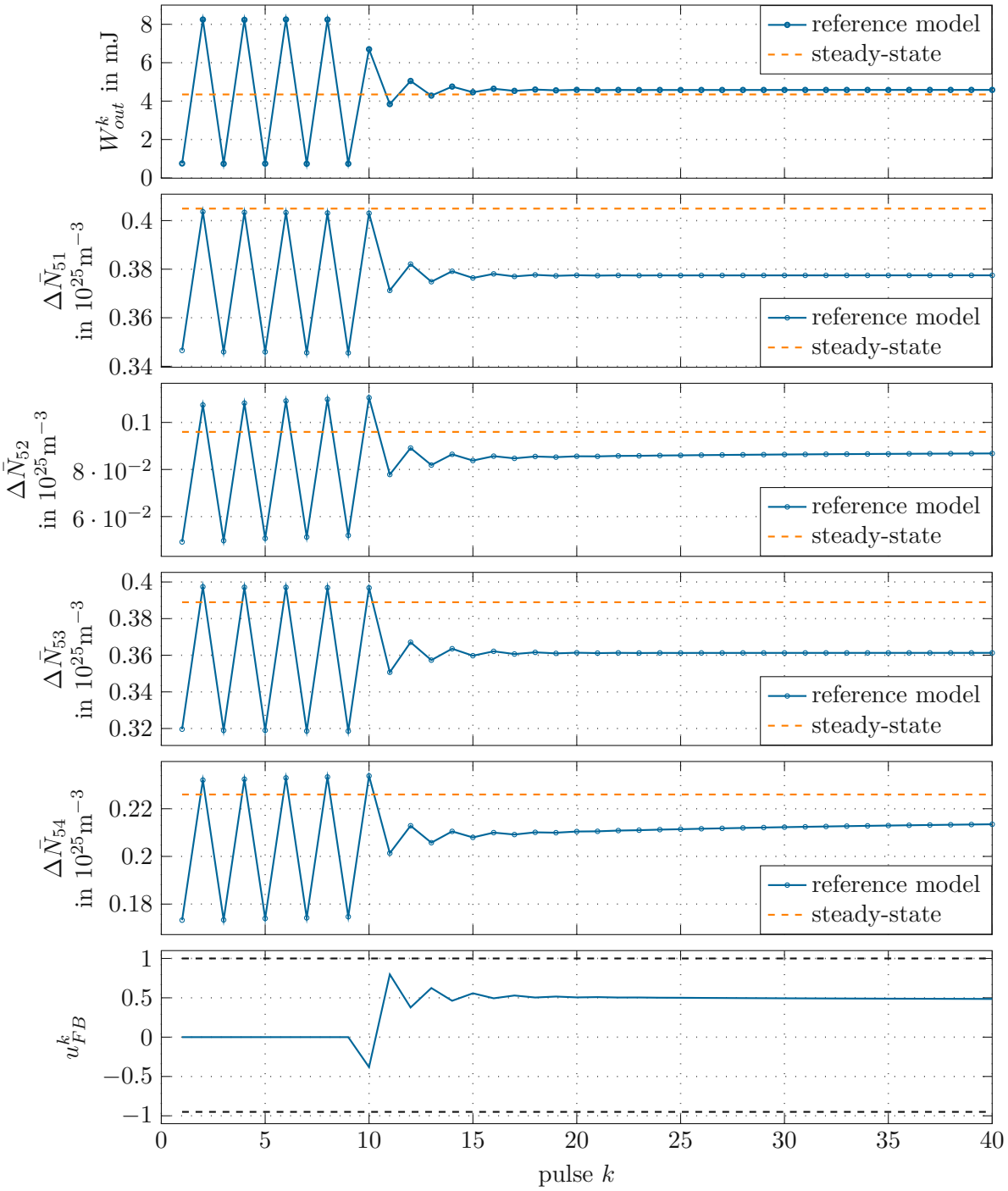

Figure 4.4: An unstable operating point being controlled by the LQR around the steady state $\bar{\mathbf{N}}^{ss}$. The unstable steady states are calculated using the steady-state equation of the reduced-order model (4.65).

the equations in (4.70) can be used to calculate the control gain matrix for the extended system. The controllability and observability of the linearized extended system (4.77) can be shown for steady states where coupling between consecutive pulses is present. Following the design in (4.70) for the extended matrices returns the control gain matrix $\mathbf{K}_{FBe}$ for the extended system

$$r^k = \mathbf{K}_{FBe} \begin{bmatrix} \Delta\bar{\mathbf{N}}^k \\ z^k \end{bmatrix}. \tag{4.78}$$

In order to keep the feedback controller input $u_{FB}^k = r^k - z^k$ inside the required constraints, $r^k \in \left(-1 + z^k; 1 + z^k\right]$ which can be enforced using a state-dependent restriction. The same simulation scenario as used in Figure 4.4 is performed with the extended controller designed with $\mathbf{Q} = \mathbf{I}$, $\mathbf{S} = \begin{bmatrix} \mathbf{0}^T & -1 \end{bmatrix}^T$ and $R = 1$. The new entry in $\mathbf{S}$ is set to -1 in order to weight the system input $u_{FB}^k = r^k - z^k$ evenly. The evolution of the pulse energy as well as the mean population inversions together with their corresponding steady states of the reduced model are plotted in Figure 4.5. Additionally the controller input values u_{FB}^k for the extended system design as well as from Figure 4.4 are plotted for comparison. This extended controller design is able to dampen excitations, but achieves a steady state closer to the calculated steady state of the reduced model and the system input u_{FB} vanishes stationary as required.

4.2 EKF-based state estimation

As discussed previously, online measurements of the populations are generally not available. Therefore, a method to estimate these populations needs to be used. In this thesis, an extended Kalman-filter (EKF) is utilized for this purpose. This section shows the derivation of an extended Kalman filter to estimate the current mean population based on the dynamics of the reduced model.

Kalman-filters are optimal state estimators [33]. They always make two estimates of the state for a given iteration k, the a-priori estimate $\bar{\mathbf{N}}_{pri}^k$ calculated before the measurement and the a-posteriori estimate $\bar{\mathbf{N}}_{post}^k$ which uses measured data to achieve a better estimate. The extended variant of the Kalman-filter uses a nonlinear model of the system dynamics to calculate the a-priori estimate $\bar{\mathbf{N}}_{pri}^k$. After the measurement, the a-priori estimate $\bar{\mathbf{N}}_{pri}^k$ is updated to the a-posteriori estimate $\bar{\mathbf{N}}_{post}^k$ using the linearized system. The EKF also incorporates information about the statistical properties of system disturbances and measurement noise. They are represented by the covariance matrix $\hat{\mathbf{Q}}$ for the system disturbance w^k and the covariance $\hat{R}$ for the measurement noise n^k, using a simple stochastic system model

$$\bar{\mathbf{N}}^{k+1} = \mathbf{F}\left(\bar{\mathbf{N}}^k, \hat{E}_{in}^{ss}(\omega)\sqrt{1 + u_{FB}^k}\right) + w^k, \tag{4.79a}$$

$$W_{out}^k = \mathrm{h}_{meas}\left(\bar{\mathbf{N}}^k, \hat{E}_{in}^{ss}(\omega)\sqrt{1 + u_{FB}^k}\right) + n^k. \tag{4.79b}$$

To get the linearized system, we use the linearization in (4.66c) around $\bar{\mathbf{N}}_{post}^k$ and (4.66d)

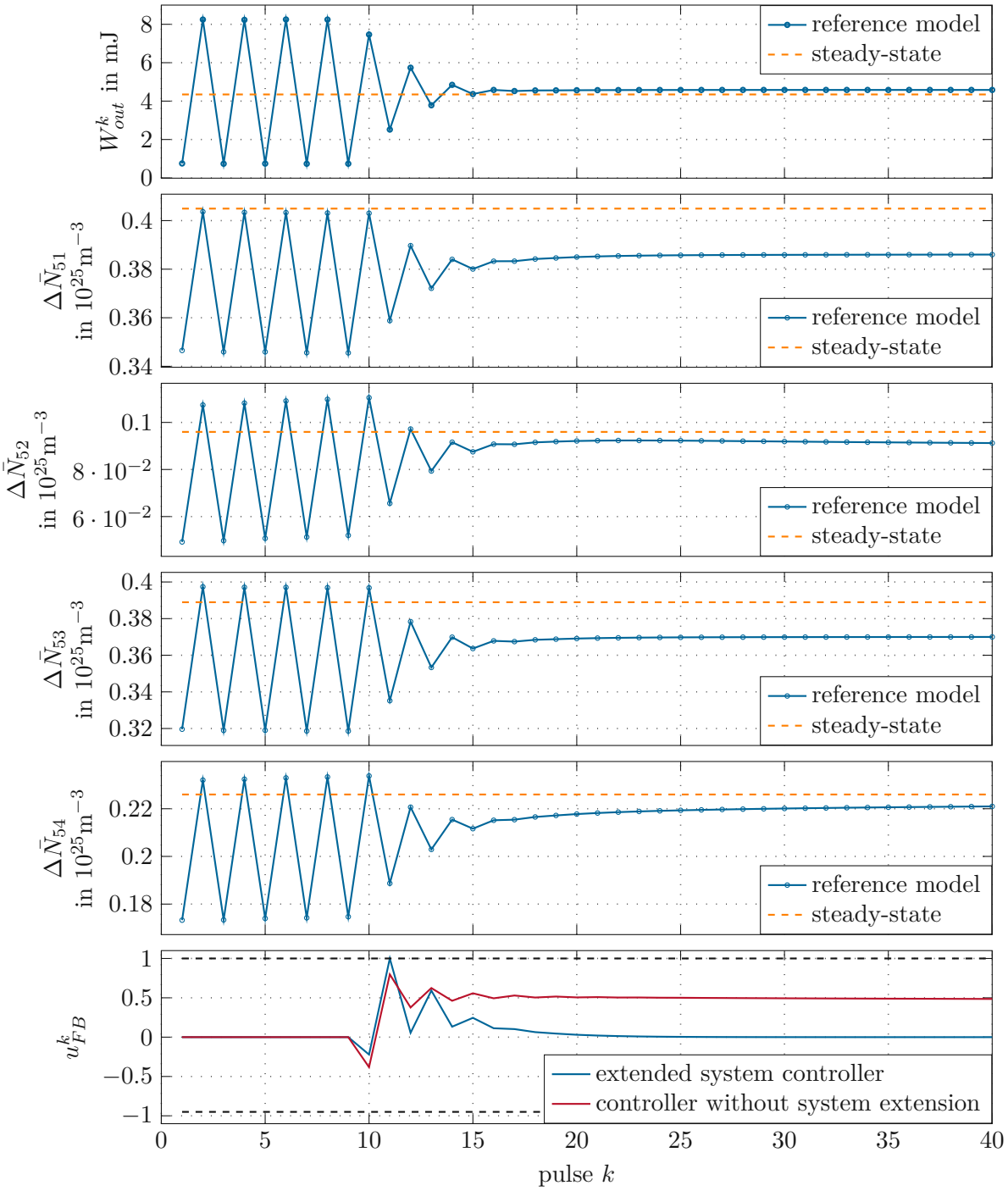

Figure 4.5: An unstable operating point being controlled by the extended system LQR, around the steady state $\bar{\mathbf{N}}^{ss}$. The unstable steady states are calculated using the steady-state equation of the reduced model (4.65).

around $\bar{\mathbf{N}}^k_{pre}$ yielding

$$\mathbf{\Phi}^k = \frac{\partial \mathbf{F}}{\partial \bar{\mathbf{N}}^k}(\bar{\mathbf{N}}^k_{post}, \hat{E}^k_{in}(\omega)) \quad \mathbf{C}^k = \frac{\partial \mathrm{h}_{meas}}{\partial \bar{\mathbf{N}}^k}(\bar{\mathbf{N}}^k_{pri}, \hat{E}^k_{in}(\omega)). \tag{4.80}$$

These derivatives are again calculated using the complex step differentiation method. For a given a-posteriori estimate $\bar{\mathbf{N}}^{(k-1)}_{post}$ of the previous state as well as the corresponding covariance matrix $\mathbf{P}^{(k-1)}_{post}$, we can calculate the best estimate of the current state using the nonlinear dynamics of the reduced model

$$\bar{\mathbf{N}}^k_{pri} = \mathbf{F}(\bar{\mathbf{N}}^{(k-1)}_{post}, \hat{E}^{(k-1)}_{in}(\omega)) \tag{4.81a}$$

and the change of the covariance matrix due to the dynamics

$$\mathbf{P}^k_{pri} = \mathbf{\Phi}^{(k-1)}\mathbf{P}^{(k-1)}_{post}(\mathbf{\Phi}^{(k-1)})^T + \hat{\mathbf{Q}}. \tag{4.81b}$$

After measuring W^k_{out} we can use the Kalman gain

$$\hat{\mathbf{L}}^k = \mathbf{P}^k_{pri}(\mathbf{C}^k)^T\Big(\mathbf{C}^k\mathbf{P}^k_{pri}(\mathbf{C}^k)^T + \hat{R}\Big)^{-1} \tag{4.81c}$$

to update the a-priori to the a-posteriori estimate

$$\bar{\mathbf{N}}^k_{post} = \bar{\mathbf{N}}^k_{pri} + \hat{\mathbf{L}}^k\Big(W^k_{out} - \mathrm{h}_{meas}(\bar{\mathbf{N}}^k_{pri}, \hat{E}^k_{in}(\omega))\Big), \tag{4.81d}$$

which is also done for the covariance matrix.

$$\mathbf{P}^k_{post} = (\mathbf{I} - \hat{\mathbf{L}}^k\mathbf{C}^k)\mathbf{P}^k_{pri}. \tag{4.81e}$$

With these estimates we can now again estimate the next state using the nonlinear dynamic of the reduced model

$$\bar{\mathbf{N}}^{(k+1)}_{pri} = \mathbf{F}(\bar{\mathbf{N}}^k_{post}, \hat{E}^k_{in}(\omega)). \tag{4.81f}$$

The set of equations in (4.81) can be implemented to estimate the current a-priori state $\mathbf{P}^k_{pri}$ used in a state feedback controller. To test the feasibility of the estimation alone, a stable operating point was simulated without the state feedback controller active, using the covariance matrices $\hat{\mathbf{Q}} = \mathrm{diag}(10^{-3}\cdot\bar{\mathbf{N}}^{ss})^2$ and $\hat{R} = (10^{-5})^2$ as well as the initial values $\mathbf{P}^0_{post} = \mathrm{diag}(10^{-3}\cdot\bar{\mathbf{N}}^{ss})^2$ and $\bar{\mathbf{N}}^0_{post} = \bar{\mathbf{N}}^{ss}$. See Figure 4.6 for the plotted estimation error propagation. This operation clearly shows that the Kalman-filter reproduces the population of the reference model quite well. Combining Kalman-filter and feedback controller and testing it on the same unstable operating point used in Figure 4.4, results in the plots of Figure 4.7. This combination is clearly able to stabilize the reference model. A comparison of the necessary control input u^k_{FB} of the EKF + LQR with the LQR alone, using the mean populations of the reference model in Figure 4.8, shows that the EKF + LQR with extension needs less control reserve while also reaching smaller control input values u^k_{FB} faster. This can be attributed to the reduced model being calibrated to the input-output behavior of the amplifier, leading to the LQR + EKF performing better than

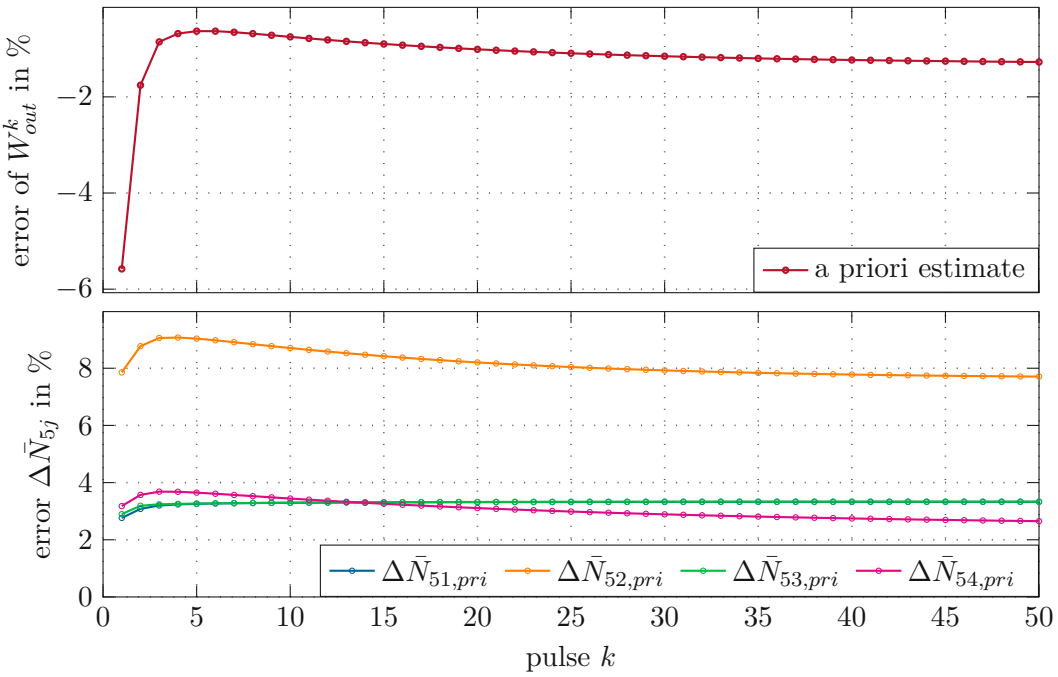

Figure 4.6: Estimation error of the EKF for the states at a stable operating point. Using $\hat{\mathbf{Q}} = \text{diag}(10^{-3} \cdot \bar{\mathbf{N}}^{ss})^2$, $\hat{R} = (10^{-5})^2$, $\mathbf{P}_{post}^0 = \text{diag}(10^{-3} \cdot \bar{\mathbf{N}}^{ss})^2$ and $\bar{\mathbf{N}}_{post}^0 = \bar{\mathbf{N}}^{ss}$.

the LQR using the populations directly, which is unusual, but is a result of the populations of the reduced-order model not being calibrated directly. Using the EKF with the LQR without extension uses a lot more control reserve and approaches a nonzero steady state, which is closer to zero than the steady state of the LQR without extension and without EKF. To test the extended LQR with the EKF, a simulation was run using different N_{RT}, f_{rep} and I_P values to achieve a variety of unstable operating points. Figure 4.9 shows the control input u_{FB} needed for systems with different maximum absolute eigenvalues $|\lambda|_{max}$. The increasing control reserve required for increasingly unstable system is clearly visible. Even with the control input u_{FB} reaching the boundaries, the combination of LQR and EKF is still able to dampen excitations of the amplifier dynamics. This ability to stabilize operating points with higher absolute eigenvalues is important because changing the input pulse shape can move the amplifier into regions with higher absolute eigenvalues during operation of the pulse shaping.

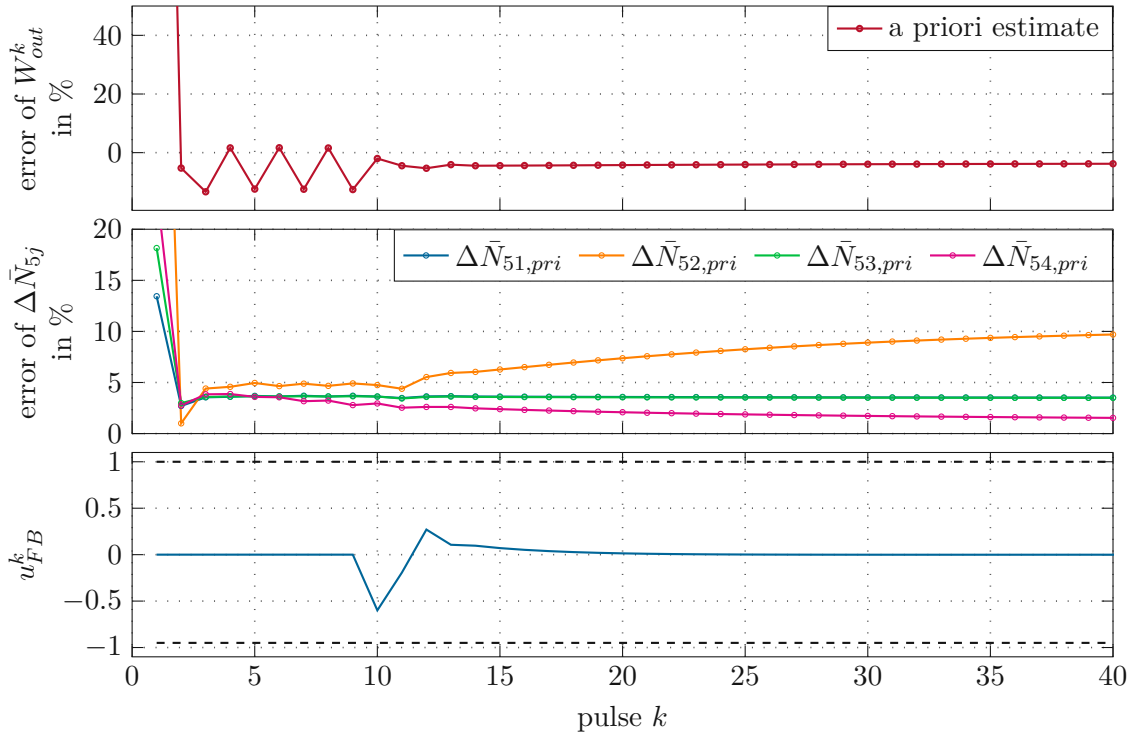

Figure 4.7: Estimation error of the EKF for the controlled system at an unstable operating point. Using $\hat{\mathbf{Q}} = \text{diag}(10^{-3} \cdot \bar{\mathbf{N}}^{ss})^2$, $\hat{R} = (10^{-5})^2$, $\mathbf{P}_{post}^0 = \text{diag}(10^{-3} \cdot \bar{\mathbf{N}}^{ss})^2$ and $\bar{\mathbf{N}}_{post}^0 = \bar{\mathbf{N}}^{ss}$.

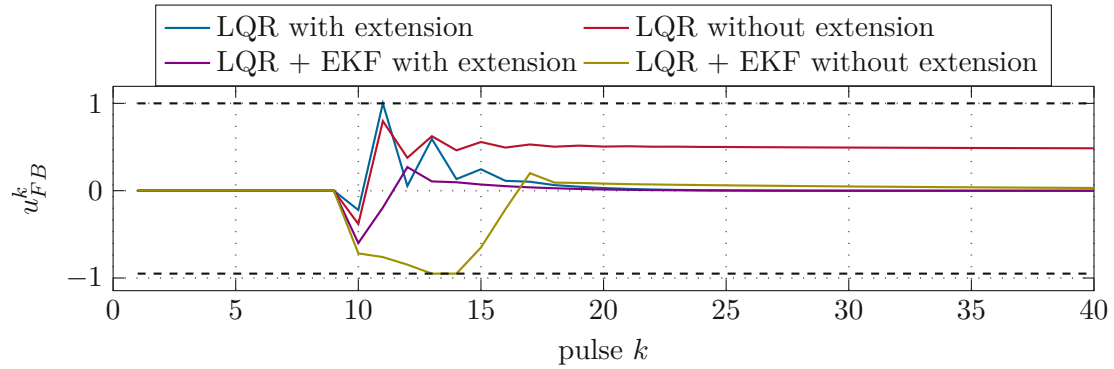

Figure 4.8: Comparison of the control input needed by the LQR with and without extension combined with and without the EKF.

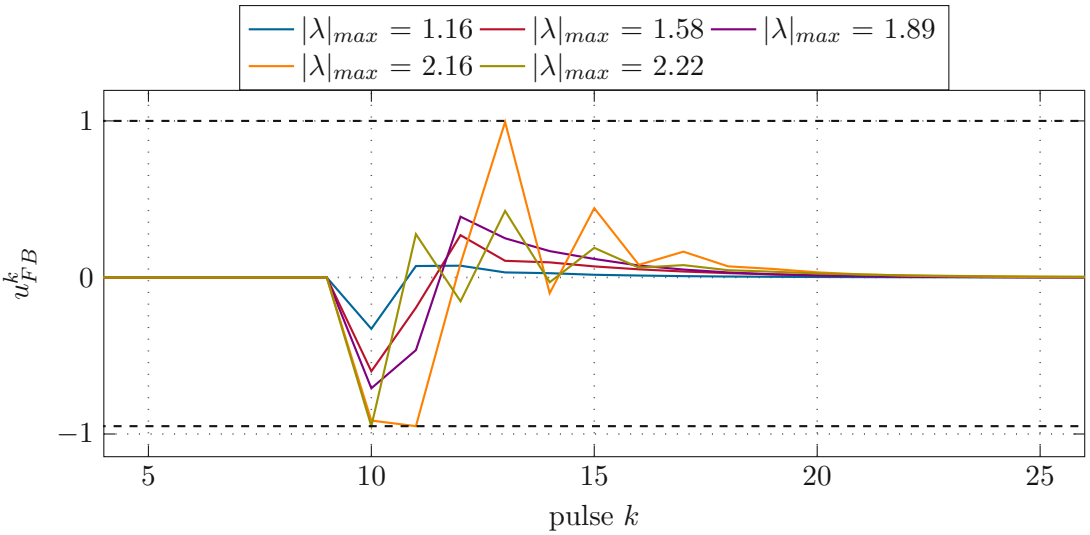

Figure 4.9: Comparison of the control input needed by the LQR with extension and EKF for different degrees of instability of the linearized dynamics, given by the maximum absolute value of the eigenvalues $|\lambda|_{max}$.

5 ILC-based spectral pulse shaping

In the previous chapter, we used u_{FB}^k to stabilize the amplifier based on measurements of the output energy W_{out}^k. The spectral shape of the resulting steady-state output pulse is thus determined by the amplifier's behavior and the chosen shape of $\hat{E}_{in}^{ss}$ in (4.60). The goal of this chapter is to use additional measurements of the output pulse $\hat{E}_{out}^k(\omega)$, available for each N_m-th pulse, to subsequently reproduce a desired pulse $\hat{E}_{out}^{des}(\omega)$ using iterative learning control (ILC) methods. To allow for an operation in unstable regimes, the ILC needs to be combined with the extended LQR and the EKF setup designed in the previous chapter.

5.1 ILC design

An intuitive way to combine these two methods is to let the ILC algorithm shape the input pulse $\hat{E}_{in}^k$ while letting the feedback controller change its energy, i.e. the input pulse for iteration k can be written as

$$\hat{E}_{in}^k(\omega) = \hat{E}_{in}^{ILC}(\omega)\sqrt{1+u_{FB}^k}. \tag{5.82}$$

Measurements of the output pulses spectral shape typically require steady-state operation of the amplifier. I.e. if the change in output energy is smaller than a threshold $W_{out,th}$ and the control input value u_{FB} is also smaller than a threshold $u_{FB,th}$, the next available output pulse measurement $\hat{E}_{out}^k(\omega)$ with $\mathrm{mod}(k, N_m) = 0$ is used to update the ILC pulse shape

$$\hat{E}_{in}^{ILC}(\omega) = \hat{E}_{in}^{ILC}(\omega) + \hat{L}^k(\omega)\Big(\hat{E}_{out}^{des}(\omega) - \hat{E}_{out}^k(\omega)\Big). \tag{5.83}$$

To force the ILC algorithm to only adapt the shape of the input pulse and not its energy, which helps to ensure a control reserve for the feedback controller, we can replace (5.83) with an energy-conserving formulation

$$\hat{E}_{in}^{ILC}(\omega) = \frac{\hat{E}_{in}^{ILC}(\omega) + \hat{L}^k(\omega)\Big(\hat{E}_{out}^{des}(\omega) - \hat{E}_{out}^k(\omega)\Big)}{\|\hat{E}_{in}^{ILC}(\omega) + \hat{L}^k(\omega)\Big(\hat{E}_{out}^{des}(\omega) - \hat{E}_{out}^k(\omega)\Big)\|}\|\hat{E}_{in}^{ILC}(\omega)\| \tag{5.84}$$

to update the ILC pulse shape. The learning operator $\hat{L}$ for both laws is designed using the pseudo-inverse-based Wien-filtering approach presented in [34] Both update laws use the same learning operator

$$\hat{L}(\omega) = d_{ILC}\frac{S(\omega)(\underline{G}_{amp}^k(\omega))^*}{\gamma_{ILC} + (\underline{G}_{amp}^k(\omega))^*\underline{G}_{amp}^k(\omega)}, \tag{5.85}$$

with a dampening parameter $d_{ILC} \in (0;1]$, a positive regularization parameter γ_{ILC}, the learning region selector $S(\omega)$ and the estimated complex spectral gain of the amplifier $\underline{G}^k_{amp}(\omega)$. The learning region selector is chosen such that learning is only done in regions where the significant gain of the amplifier is required, i.e.

$$S(\omega) = \begin{cases} 1 & |\hat{E}_{out,des}(\omega)| \geq 10^4 \max |\hat{E}_{out,des}(\omega)| \\ 0 & else \end{cases}. \tag{5.86}$$

To calculate the complex spectral gain $\underline{G}_{amp}(\omega)$, we can exploit the special form of the output map (2.40b) of the reduced model

$$\hat{E}^k_{out}(\omega) = \mathrm{h}(\bar{\mathbf{N}}^k, \hat{E}^k_{in}(\omega)) = \underline{G}_{amp}(\omega, \bar{\mathbf{N}}^k, \hat{E}^k_{in}(\omega))\hat{E}^k_{in}(\omega) \tag{5.87}$$

which is a direct result of (2.29b) and (2.32). For given $\bar{\mathbf{N}}^k$, $\hat{E}^k_{in}(\omega)$ and $\hat{E}^k_{out}(\omega)$ this equation can easily be solved for $\underline{G}_{amp}(\omega, \bar{\mathbf{N}}^k, \hat{E}^k_{in}(\omega))$. After each update the LQR needs to be recalculated, since the underlying linearization depends on the spectral shape of the current input pulse.

Now we only need to choose a suitable initial shape $\hat{E}^{ILC}_{in}(\omega)$ for the ILC algorithm. A simple choice would be the same as used in testing the control algorithms in the previous chapter, i.e. $\hat{E}^{ILC}_{in}(\omega) = \frac{1}{\sqrt{2}}\hat{E}_{seed}(\omega)$,. For a more sensible initial choice, we can use the gain equation in (5.87). By neglecting the influence that $\hat{E}^k_{in}(\omega)$ has on $\underline{G}_{amp}(\omega, \bar{\mathbf{N}}^k, \hat{E}^k_{in}(\omega))$, i.e. neglecting the reduction in population during amplification, we can get the initial input pulse $\hat{E}^{ILC}_{in}(\omega)$ and the corresponding steady-state population of the reduced model by solving

$$\bar{\mathbf{N}}^{ss} = \mathbf{F}(\bar{\mathbf{N}}^{ss}, \hat{E}^{ILC}_{in}(\omega)) \tag{5.88a}$$

$$\hat{E}^{des}_{out}(\omega) = G_{us}(\omega, \bar{\mathbf{N}}^{ss})\hat{E}^{ILC}_{in}(\omega) = \eta^{N_{RT}}_{RC} f^{N_{RT}}_E(\bar{\mathbf{N}}^{ss}, \hat{E}^{ILC}_{in}(\omega)), \tag{5.88b}$$

with f_E from (2.29b), for the steady-state population $\bar{\mathbf{N}}^{ss}$ and then solving (5.88b) for the initial pulse $\hat{E}^{ILC}_{in}(\omega)$. The second method produces good initial guesses for the ILC algorithm, in particular for stable operating points. All following simulations of the ILC use the first method to better show the convergence of the ILC for stable operating points. The full implemented ILC algorithm can now be assembled. A flow diagram of the whole system is depicted in Figure 5.1.

5.2 Simulation scenarios

Multiple operating points, both stable and unstable, were tested to validate the developed algorithm's functionality. A stable and an unstable operating point are presented in more detail here.

5.2.1 Stable operating point with energy-normalized learning

To get a stable operating point, the amplifier is operated with a pump intensity $I_P = 155\,\mathrm{W/mm^2}$, with the seed pulse source set to $f_{rep} = 10\,\mathrm{kHz}$ and each pulse amplified for

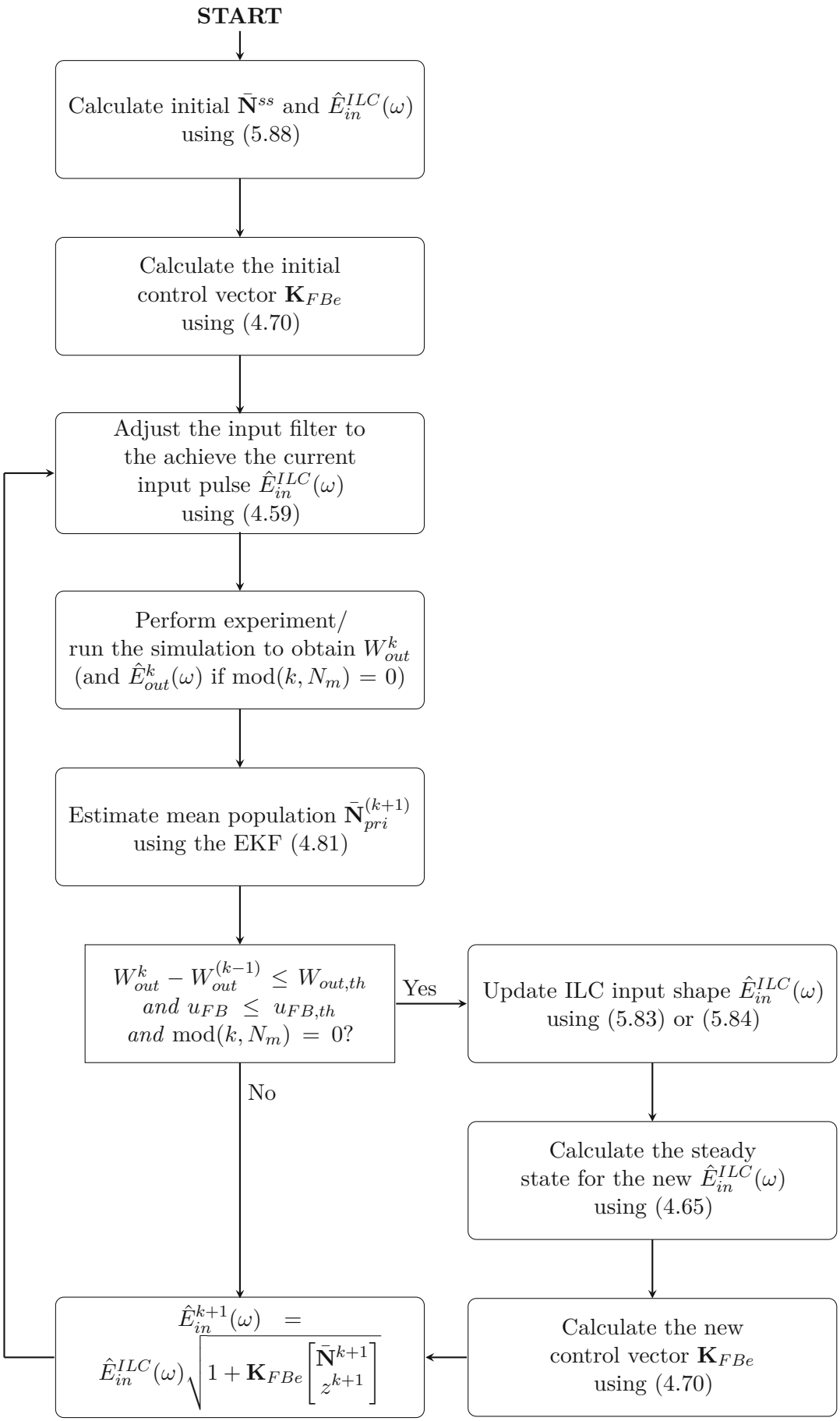

Figure 5.1: Flow diagram of the ILC algorithm including the EKF as well as the adaptation of the extended LQR.

$N_{RT} = 17$ round trips. A desired output pulse in the shape of a Gaussian distribution and an energy of $W_{out}^{des} = 79\,\mu J$ is chosen. As discussed in the previous section, (5.1) is used to calculate the initial ILC pulse shape which is updated using the energy-normalized learning in (5.84). The amplifier is initially in steady-state operation and the EKF is activated at $k = 0$ using the same parameters as in Figure 4.6 and the LQR is activated at $k = 10$ after the estimation error converged with the same parameters as in Figure 4.5. The linearized system dynamics of the reduced model has eigenvalues with a maximum absolute value of 0.9730. The full spectral measurements of $\hat{E}_{out}^{k}(\omega)$ necessary for these updates are assumed to be available every fifth pulse, i.e. $N_m = 5$. To classify the deviation of the output pulse from its desired shape, we can use the relative pulse energy error

$$e_{pulse}^{k} = \frac{\int_{-\infty}^{\infty} |\hat{E}_{out}(\omega)^k - \hat{E}_{des}(\omega)|^2 d\omega}{\int_{-\infty}^{\infty} |\hat{E}_{des}(\omega)|^2 d\omega}. \tag{5.89}$$

Figure 5.2 presents the results of this simulation scenario. The ILC algorithm is clearly able to reduce the relative pulse energy error using the update law (5.84), these update steps are visible at pulse 20, 30, 40, 50, 55 and so on in Figure 5.2b. The updates start getting ineffective after pulse 100, which can be attributed to the pulse having too much energy. While the pulse's shape is matching the desired pulse, the energy-normalized learning is not adjusting the total energy.

5.2.2 Unstable operating point with energy-normalized learning

A similar simulation scenario with an unstable operating point is achieved by using a higher number of round trips $N_{RT} = 35$, while keeping the pump intensity at $I_P = 155\,W/mm^2$ and the seed pulse frequency at $f_{rep} = 10\,kHz$. Since this operation achieves higher pulse energy gain, a desired pulse with the same shape and an energy of $W_{out}^{des} = 514\,\mu J$ was used. With the same simple initial pulse shape (5.1), this results in a linearized system with features a maximum absolute eigenvalue of 1.6987. See Figure 5.3 for the results of this simulation scenario. These plots clearly show that the LQR stabilizes the amplifier. The ILC updates at pulse 45, 55, 65, 70 and so on only introduces minor dynamic excitations due to the energy-normalized learning. Once again, these learning updates start becoming ineffective after pulse 120, but they are still visible in Figure 5.3b because of the excitation of the amplifier dynamics. The output pulse strongly deviates in Figure 5.3a from the desired pulse, which can mainly be attributed to the achieved output energy being too high, which the ILC can only influence slightly due to the energy-normalized learning.

5.2.3 Stable and unstable operation without energy-normalizing learning

Using the same operating parameters from the previous two simulations but swapping from the energy normalizing ILC update law (5.84) to the ILC update law without energy normalization (5.83), i.e. letting the ILC influence the input pulse energy, results in the two simulations presented next. The results of the stable operating point are plotted in Figure 5.4. This operation achieves the goal of the output pulse $\hat{E}_{out}^{k}(\omega)$ converging to the desired output pulse $\hat{E}_{out}^{k}(\omega)$, with the smallest e_{pulse}^{k} values reaching around 0.04%.

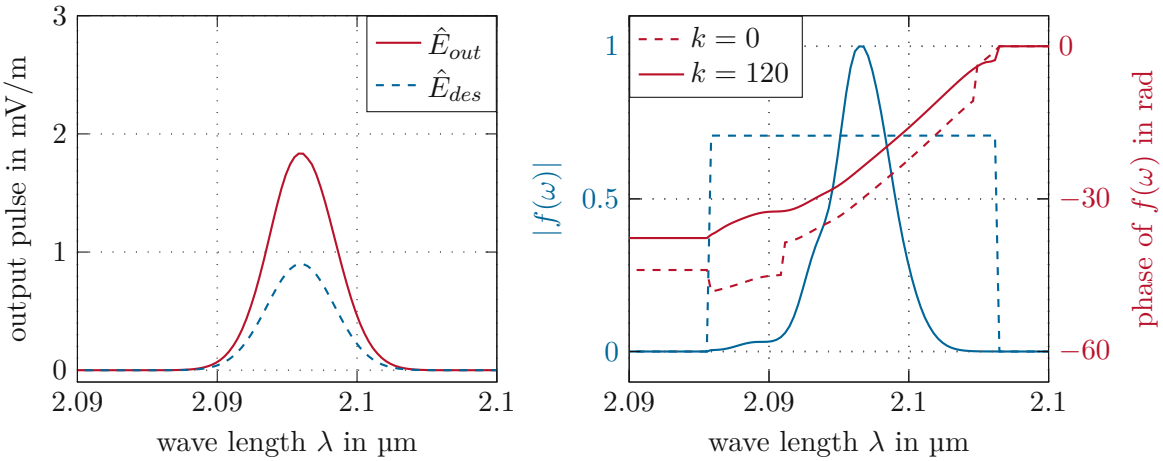

(a) The output pulse $\hat{E}^k_{out}(\omega)$ compared to the desired pulse $\hat{E}^{des}_{out}(\omega)$ as well as the initial and end filter settings of $f(\omega)$.

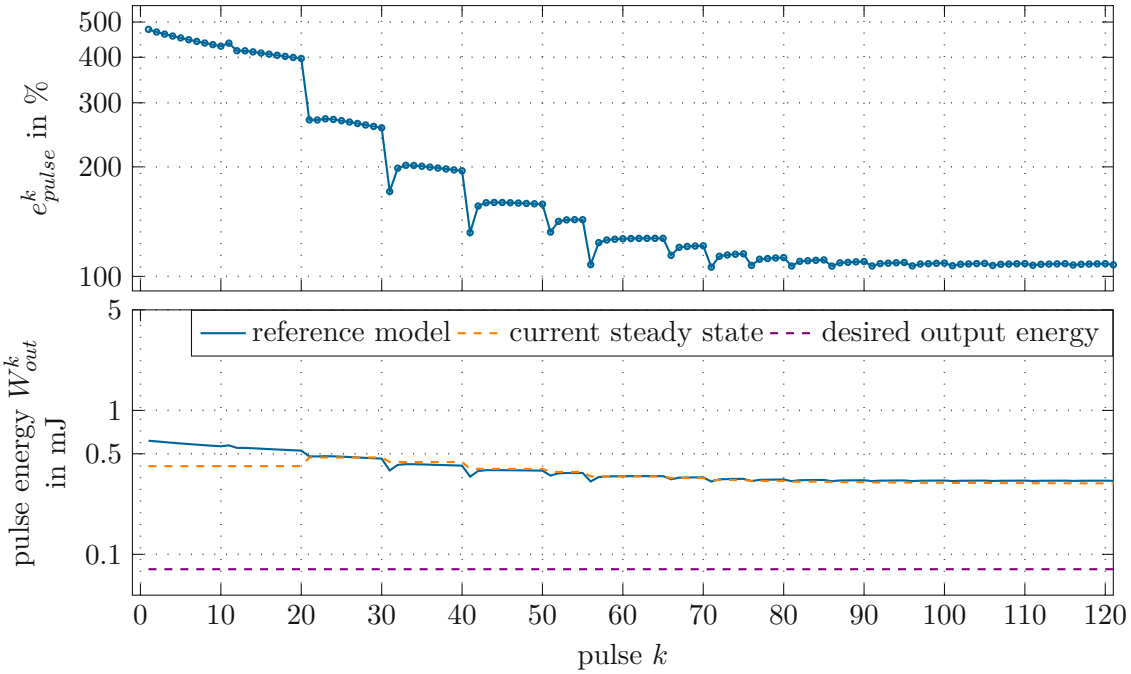

(b) Evolution of the relative pulse energy error e^k_{pulse} and output energy W^k_{out}. The output energy plot also shows the output energy of the current steady state of the reduced model as well as the desired pulse energy.

Figure 5.2: ILC convergence for a stable operating point with energy-normalized learning (5.84)-logarithmic scaling.

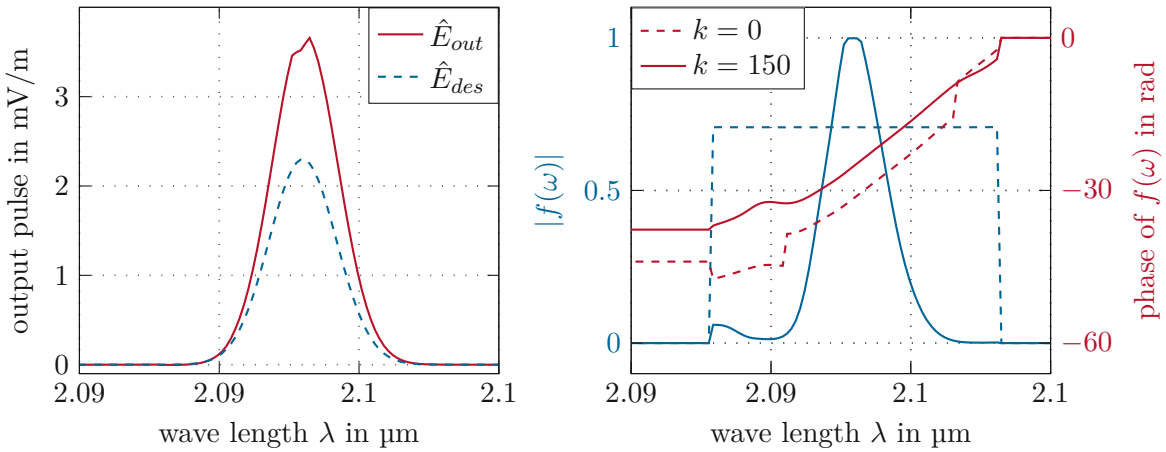

(a) The output pulse $\hat{E}^k_{out}(\omega)$ compared to the desired pulse $\hat{E}^{des}_{out}(\omega)$ as well as the initial and end filter settings of $f(\omega)$.

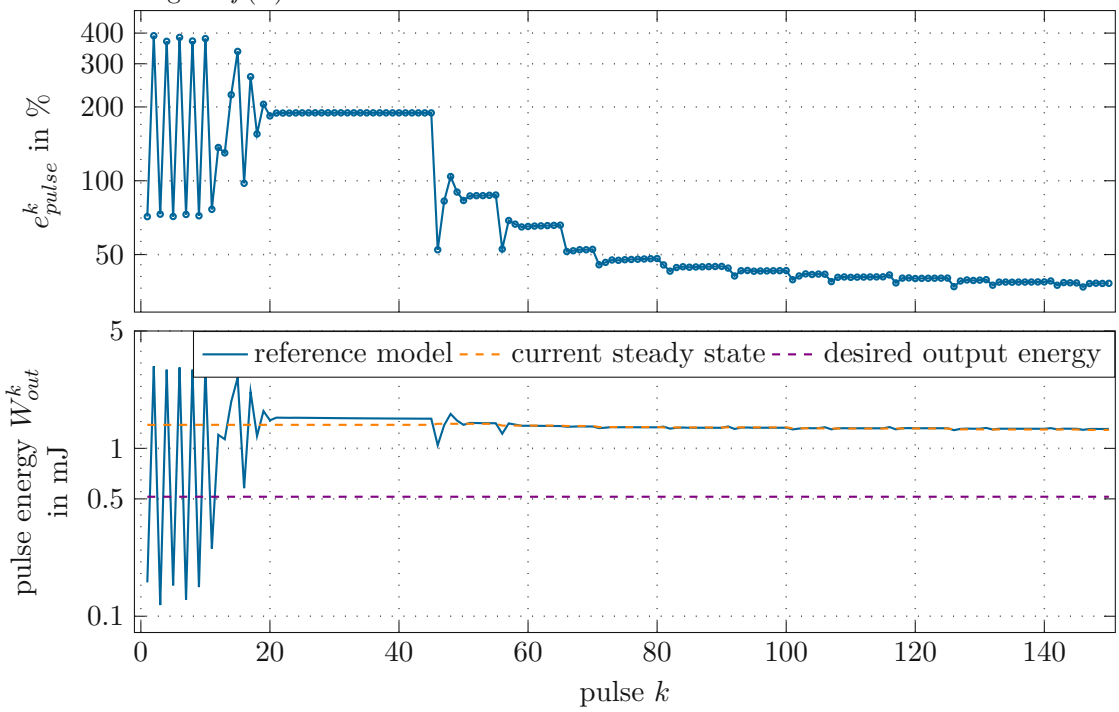

(b) Evolution of the relative pulse energy error e^k_{pulse} and output energy W^k_{out}. The output energy plot also shows the output energy of the current steady state of the reduced model as well as the desired pulse energy.

Figure 5.3: ILC convergence for an unstable operating point with energy-normalized learning (5.84)-logarithmic scaling

The only problem with this operation are the small absolute values of $f(\omega)$ necessary to achieve this operating point, which are generally not achievable with reasonable accuracy by optical filters. This problem is even more pronounced for the unstable operating point, with the necessary absolute value of the input filter being nearly indistinguishable from zero in Figure 5.5.

5.2.4 Reduced pump intensity

Another more applicable option to reduce the output energy of the amplifier is to reduce the pump intensity I_P of the pumping beam. For example, reducing it from $I_P = 155\,\mathrm{W/mm^2}$ to $I_P = 24\,\mathrm{W/mm^2}$ in Section 5.2.1 and still using the same initial ILC pulse shape combined with the energy-altering ILC update (5.83) results in the output pulse and input filter spectra presented in Figure 5.6. Looking at the absolute value of the filter, we can see that more control reserve is used, just as desired while still reducing the relative pulse energy error e^k_{pulse} to values below 0.01%. Actively controlling the quantity I_P as an additional input, such that the output energy of the stead state W^{ss}_{out} matches the desired output energy W^{des}_{out} using a feedback controller should achieve better convergence of the ILC while keeping the input filter in a usable operating region. It can also be used to keep the learned input shape $\hat{E}^{ILC}_{in}(\omega)$ in a range such that the full control reserve $u_{FB} \in (-1; 1]$ is always available within the input filter constraints.

The presented ILC algorithm combined with the extended LQR controller and EKF is clearly able to suppress bifurcation while simultaneously correcting the pulse shape within the physical limits of the amplifier. Since the reference model closely matches a (Ho:YAG) laser amplifier, we can expect the ILC to also work on a real-life implementation.

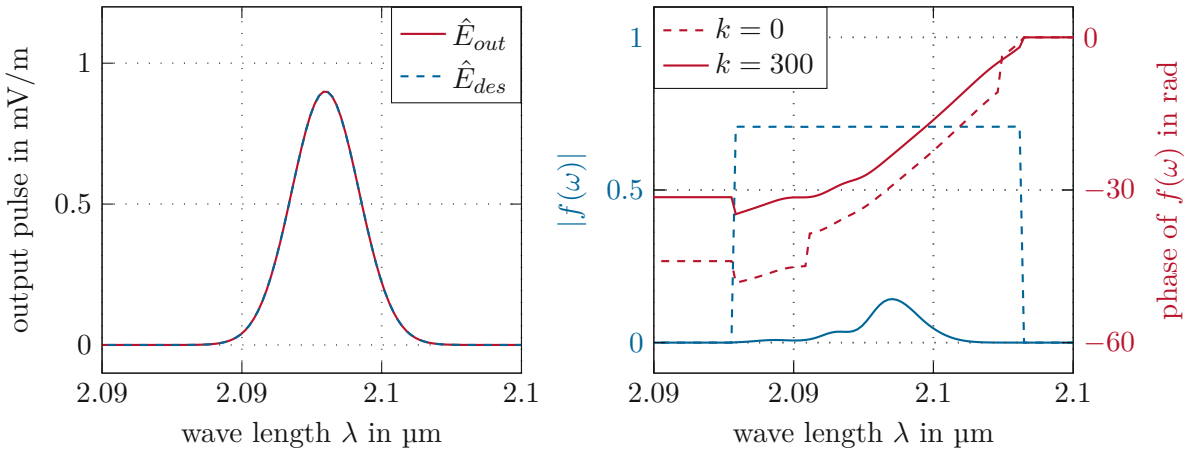

(a) The output pulse $\hat{E}^k_{out}(\omega)$ compared to the desired pulse $\hat{E}^{des}_{out}(\omega)$ as well as the initial and end filter settings of $f(\omega)$.

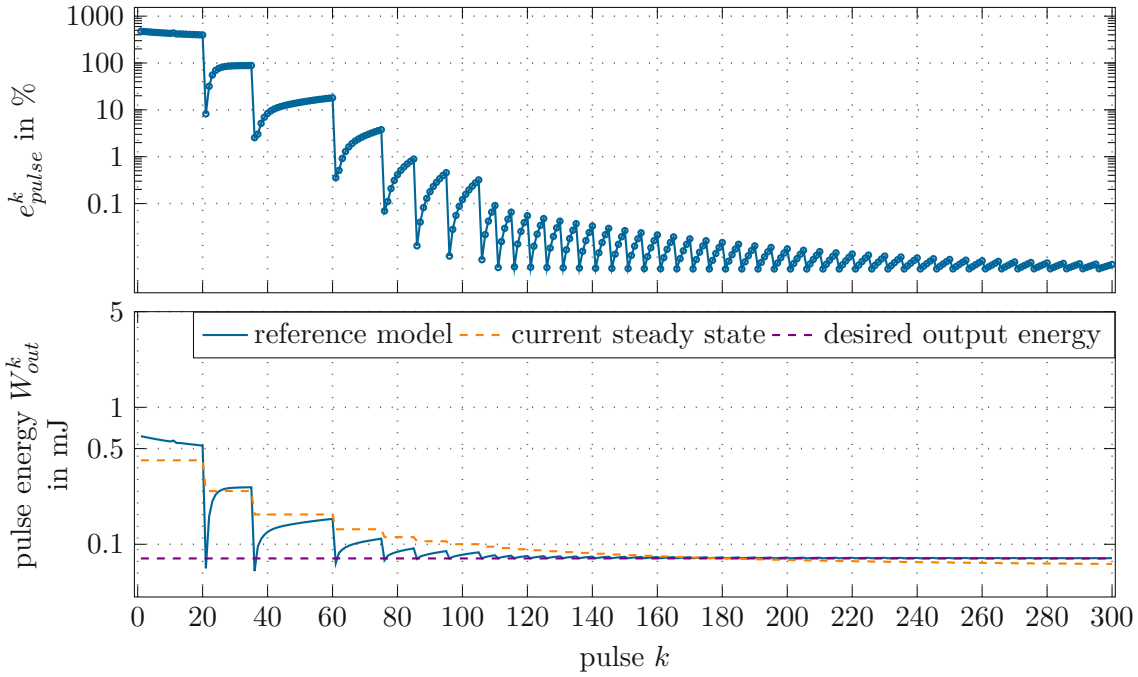

(b) Evolution of the relative pulse energy error e^k_{pulse} and output energy W^k_{out}. The output energy plot also shows the output energy of the current steady state of the reduced model as well as the desired pulse energy.

Figure 5.4: ILC convergence for a stable operating point with energy-altering learning (5.83)-logarithmic scaling.

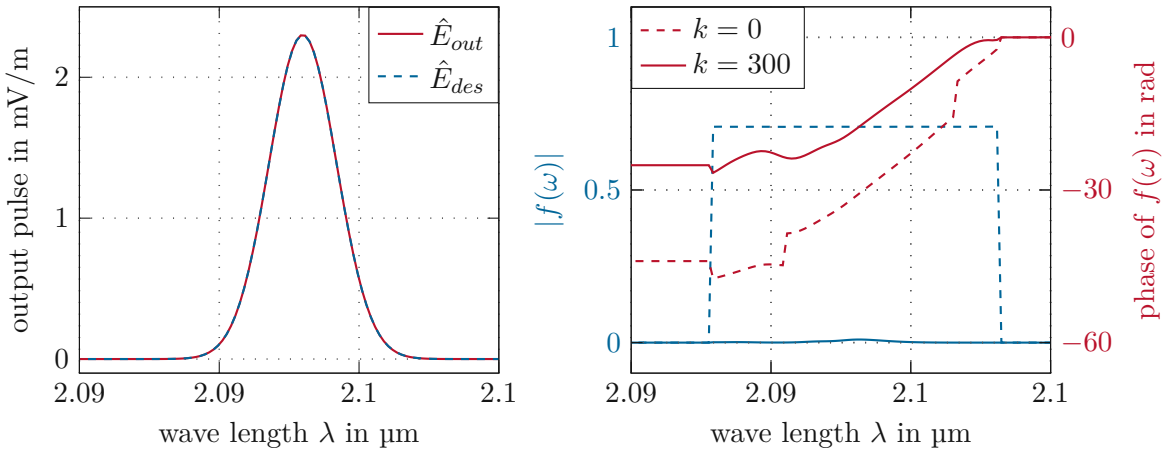

Figure 5.5: The output pulse $\hat{E}^k_{out}(\omega)$ compared to the desired pulse $\hat{E}^{des}_{out}(\omega)$ as well as the initial and end filter settings of $f(\omega)$ for an unstable operating point with energy-altering learning (5.83).

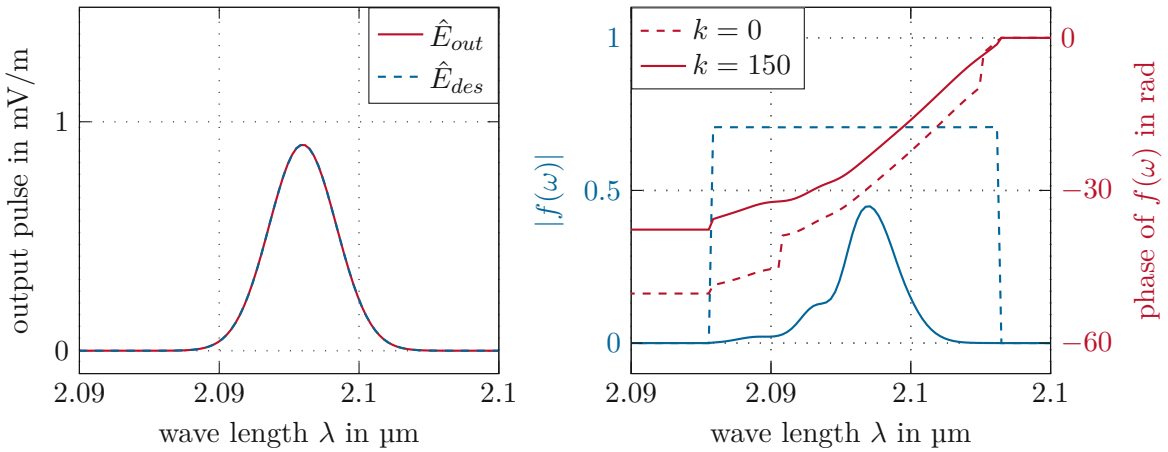

Figure 5.6: The output pulse $\hat{E}^k_{out}(\omega)$ compared to the desired pulse $\hat{E}^{des}_{out}(\omega)$ as well as the initial and end filter settings of $f(\omega)$ for a stable operating point with reduced pump intensity and energy-altering learning (5.84).

6 Conclusions and Outlook

The main goal of this thesis was to extend existing pulse-shaping schemes for regenerative amplifiers (RAs) to dynamically unstable operating points. To this end, a reduced dynamic model of RAs was derived in Chapter 2. This was done by using the Fourier space to linearly approximate the amplification of a pulse propagating through the gain medium while using this approximation to estimate the amount of population being lost due to this amplification. In combination with the population change due to the pumping during the regeneration phase between two pulses, this model can reproduce the dynamics and the spectral behavior of regenerative amplifiers using a nonlinear discrete-time dynamic system. After calibration to steady-state output measurements in Chapter 3, this model can be used to design a state estimator and a state feedback controller in Chapter 4 to suppress the bifurcation of the RA. Pulse shaping through iterative learning control (ILC) methods can subsequently be applied to the feedback-stabilized amplifier in Chapter 5. This combined application of state feedback control and ILC was shown to be able to suppress bifurcation and achieve output pulse shaping, while still being applicable to open-loop stable operating points. The implemented pulse shaping still has some problems if the pump light intensity and thus the operating point is chosen poorly for the desired output pulse, the presented algorithms either fail to deliver the desired energy or lead to unreasonable input pulse values. By adding the pump intensity as a (slowly) adjustable control input, the presented scheme could be augmented to deliver stable pulses of desired shape and energy.

In addition to this, different types of model predictive control could also be applied. This should enable us to take input (and other safety) constraints systematically into account. The application of other optimal estimation methods, such as unscented Kalman filters and Bayesian state estimation methods, could also be explored further.

Since the testing of the developed bifurcation suppression and pulse shaping algorithm is only done using simulation, testing the proposed concept on a real amplifier would also be desirable, since these implementations generally reveal additional challenges. The implemented algorithm's robustness to measurement noise can then also be investigated.

Overall, the reduced model shows good performance in pulse shaping while not being numerically expensive, making online operation of such an algorithm possible. The calibration method could also be used in a startup initialization since it only uses a variety of steady-state measurements, which can be measured during operation.

A Appendix

A.1 Slowly varying envelope approximation

The slowly varying envelope approximation (SVEA) assumes that the envelope of a propagating pulse is varying slowly in time and space compared to the carrier frequency and wavelength, respectively [1]. For a wave in the form

$$\mathcal{A}(z,t) = A(z,t)\exp\Big[i(\omega_0 t - k_0 z)\Big], \tag{A.90}$$

we can write this using the two temporal approximations

$$\left|\frac{\partial A(z,t)}{\partial t}\right| \ll \Big|\omega_0\, A(z,t)\Big| \tag{A.91}$$

and

$$\left|\frac{\partial^2 A(z,t)}{\partial^2 t}\right| \ll \left|\omega_0\,\frac{\partial A(z,t)}{\partial t}\right| \ll \Big|\omega_0^2\, A(z,t)\Big|. \tag{A.92}$$

Further, the two spatial approximations are given by

$$\left|\frac{\partial A(z,t)}{\partial z}\right| \ll \Big|k_0\, A(z,t)\Big| \tag{A.93}$$

and

$$\left|\frac{\partial^2 A(z,t)}{\partial^2 z}\right| \ll \left|k_0\,\frac{\partial A(z,t)}{\partial z}\right| \ll \Big|k_0^2\, A(z,t)\Big|. \tag{A.94}$$

These approximations can be used to reduce the complexity of spatial and temporal derivatives of the wave function in (A.90). For example, if we apply the second time derivative we get

$$\frac{\partial^2 \mathcal{A}(z,t)}{\partial t^2} = \frac{\partial^2}{\partial t^2}\left(A(z,t)\exp\Big[i(\omega_0 t - k_0 z)\Big]\right), \tag{A.95}$$

using the product rule twice yields

$$\frac{\partial^2 \mathcal{A}(z,t)}{\partial t^2} = \left(\frac{\partial^2 A(z,t)}{\partial^2 t} + i2\omega_0\,\frac{\partial A(z,t)}{\partial t} - \omega_0^2\, A(z,t)\right)\exp\Big[i(\omega_0 t - k_0 z)\Big]. \tag{A.96}$$

By using the temporal approximations we can simplify this to

$$\frac{\partial^2 \mathcal{A}(z,t)}{\partial t^2} \approx -\omega_0^2\, A(z,t)\exp\Big[i(\omega_0 t - k_0 z)\Big]. \tag{A.97}$$

This can also be applied to the spatial derivatives

$$\frac{\partial^2 \mathcal{A}(z,t)}{\partial z^2} \approx -k_0^2\, A(z,t)\exp\Big[i(\omega_0 t - k_0 z)\Big]. \tag{A.98}$$

A.2 Selected Fourier transform identities

The following identities [35] have been used extensively in this thesis. The Fourier transform of a time derivative read as

$$\mathcal{F}\left[\frac{\partial f(t)}{\partial t}\right](\omega) = i\omega\, \mathcal{F}[\partial f(t)]. \tag{A.99}$$

The integral over the time function corresponds to the zero frequency component of the Fourier transform

$$\int_{-\infty}^{\infty} f(t)dt = \mathcal{F}[f(t)](\omega)\Big|_{\omega=0}. \tag{A.100}$$

To calculate the Fourier transform of the complex conjugate of a time function, we can use

$$\mathcal{F}[f^*(t)](\omega) = \mathcal{F}[f(t)]^*(-\omega). \tag{A.101}$$

The Fourier transform of a product of time functions can be calculated using the convolution of the Fourier transformed functions

$$\mathcal{F}[f(t)g(t)](\omega) = \int_{-\infty}^{\infty} \mathcal{F}[f(t)](\omega')\mathcal{F}[g(t)](\omega-\omega')d\omega'. \tag{A.102}$$

A.3 Complex step differentiation method

A few different numerical methods are available to calculate the derivative of a function $f(p)$ with respect to a parameter p. Most of these are based on the Taylor series expansion with the step width h

$$f(p+h) = f(p) + h\frac{\partial f(p)}{\partial p} + \frac{h^2}{2}\frac{\partial^2 f(p)}{\partial p^2} + \frac{h^3}{6}\frac{\partial^3 f(p)}{\partial p^3} + \frac{h^4}{24}\frac{\partial^4 f(p)}{\partial p^4} + \dots \quad . \tag{A.103}$$

Among these are the forward and backward difference methods

$$\frac{\partial f(p)}{\partial p} \approx \frac{1}{h}\Big(f(p+h) - f(p)\Big), \tag{A.104}$$

and

$$\frac{\partial f(p)}{\partial p} \approx \frac{1}{h}\Big(f(p) - f(p-h)\Big), \tag{A.105}$$

both of which have an error scaling with h^2. Another typical method is the central difference

$$\frac{\partial f(p)}{\partial p} \approx \frac{1}{2h}\Big(f(p+h) - f(p-h)\Big), \tag{A.106}$$

which has an error that scales with h^3. For values of $h \ll 1$, higher orders of the error are usually advantageous. All these methods share the problem of elimination which originates from the subtraction involved in all of them. This means that for large values of $f(p)$ and small values of h the difference can be around the computational numerical accuracy of the number system used, leading to inaccurate estimates of the derivative. For holomorphic functions [36], a different method without this problem is available. It uses the Taylor series expansion with a complex step ih

$$f(p+ih) = f(p) + ih\frac{\partial f(p)}{\partial p} - \frac{h^2}{2}\frac{\partial^2 f(p)}{\partial p^2} - i\frac{h^3}{6}\frac{\partial^3 f(p)}{\partial p^3} + \frac{h^4}{24}\frac{\partial^4 f(p)}{\partial p^4} + \dots \quad . \tag{A.107}$$

By taking the imaginary part of this expansion, we get

$$\mathrm{Im}\Big\{f(p+ih)\Big\} = h\frac{\partial f(p)}{\partial p} - \frac{h^3}{6}\frac{\partial^3 f(p)}{\partial p^3} + \dots \quad , \tag{A.108}$$

and thus an approximation of the first derivative is given by

$$\frac{\partial f(p)}{\partial p} \approx \frac{1}{h}\mathrm{Im}\Big\{f(p+ih)\Big\}, \tag{A.109}$$

which has an error that scales with h^3. Since no subtraction of the evaluated function is calculated, the problem of elimination does not arise.

A.4 Steady-state calibration variants

The steady-state calibration uses two parameters which change the operating point and therefore the steady state of the system, i.e. the input energy W_{in} and the pump intensity I_P. To get robust calibration results, a combination of multiple of these parameters have to be used. However, the number and range required is a-priori unclear. Thus, a number of variants is explored in the following. A detailed overview of the parameters used for the different calibration versions is shown in Table A.1. The parameters I_P and W_{in} are presented as factors f_I and f_W of the reference values $I_{P,ref} = 119\,\mathrm{MW/m^2}$ and $W_{ref} = 2\,\mathrm{mJ}$, i.e., $I_P = I_{P,ref} f_I$ and $W_{in} = W_{ref} f_W$.

Since the different calibration variants use different numbers of points, the value of the cost function J to compare the results is not practical. We therefore need to introduce a new metric for comparison. To achieve this, a 15 by 15 grid of steady states for the reference model was calculated. By calculating the root mean squared value of the relative error between the reduced model for each calibration and these steady states using

$$e_{RMS,X} = \sqrt{\frac{1}{15\cdot 15}\sum_{i=1}^{15}\sum_{j=1}^{15}\Big(\frac{X_{ss,ref,ij} - X_{ss,red,ij}}{X_{ss,ref,ij}}\Big)^2}, \tag{A.110}$$

Table A.1: Input values used for the different calibration variants. With the number of parameters as well as min and max values of these parameters if multiple are used. The parameters are presented as factors of the reference values. Variant 1 and 18 seem identical, but the f_I values where chosen linearly in Variant 1 and logarithmic (except for 0) in Variant 18.

Variant	$N_{W_{in}}$	f_W	N_{I_P}	f_I
1	1	1	5	0 to 2
2	1	3	5	0 to 2
3	1	$1/3$	5	0 to 2
4	1	1	3	0 to 2
5	1	1	10	0 to 2
6	2	$1/2$ to 2	5	0 to 2
7	3	$1/4$ to 2	5	0 to 2
8	3	$1/20$ to 2	5	0 to 2
9	3	$1/100$ to 2	5	0 to 2
10	5	$1/20$ to 2	5	0 to 2
11	5	$1/20$ to 2	5	0 to 2
12	7	$1/100$ to 2	5	0 to 2
13	1	1	5	0 to 1
14	1	1	3	0 to 1.3
15	3	$1/100$ to 2	3	0 to 2
16	3	$1/3$ to 2	3	0 to 2
17	1	1	3	0 to 2
18	1	1	5	0 to 2
19	1	$3/2$	5	0 to 2
20	1	$3/4$	5	0 to 2

we can get a value that does not depend on the number of steady states. This value is calculated for all the split energies $X \in \{W_1, W_2, W_3, W_4\}$ as well as the full energy W_{out}. To reduce the amount of metrics the combined RMS value and the combined RMS value of the split energies are calculated

$$e_{RMS,comb} = \sqrt{e^2_{RMS,W_1} + e^2_{RMS,W_2} + e^2_{RMS,W_3} + e^2_{RMS,W_4} + e^2_{RMS,W_{out}}} \tag{A.111}$$

and

$$e_{RMS,comb,split} = \sqrt{e^2_{RMS,W_1} + e^2_{RMS,W_2} + e^2_{RMS,W_3} + e^2_{RMS,W_4}}. \tag{A.112}$$

Every variant of the chosen calibration points was run four times using different calibration parameters:

1. without calibrating the three relaxation probability values $\{\gamma_{02}, \gamma_{03}, \gamma_{04}\}$ and without using the full energy W_{out} inside the cost function $J(p)$.
2. with the relaxation probabilities $\{\gamma_{02}, \gamma_{03}, \gamma_{04}\}$ as calibration variables, also without the full energy W_{out} in the cost function $J(p)$.
3. not calibrating the relaxation probabilities $\{\gamma_{02}, \gamma_{03}, \gamma_{04}\}$, but with the full energy W_{out} in the cost function $J(p)$.
4. with both, the relaxation probabilities $\{\gamma_{02}, \gamma_{03}, \gamma_{04}\}$ as calibration values and the full energy W_{out} inside the cost function $J(p)$.

The resulting RMS values of the different variants are displayed in Figure A.1 and the combined RMS values is in Figure A.2. To better compare the bar heights, the minimum value is displayed as a line in every plot. Because the lowest combined RMS value was achieved for variant 6, it was chosen as the best calibration result.

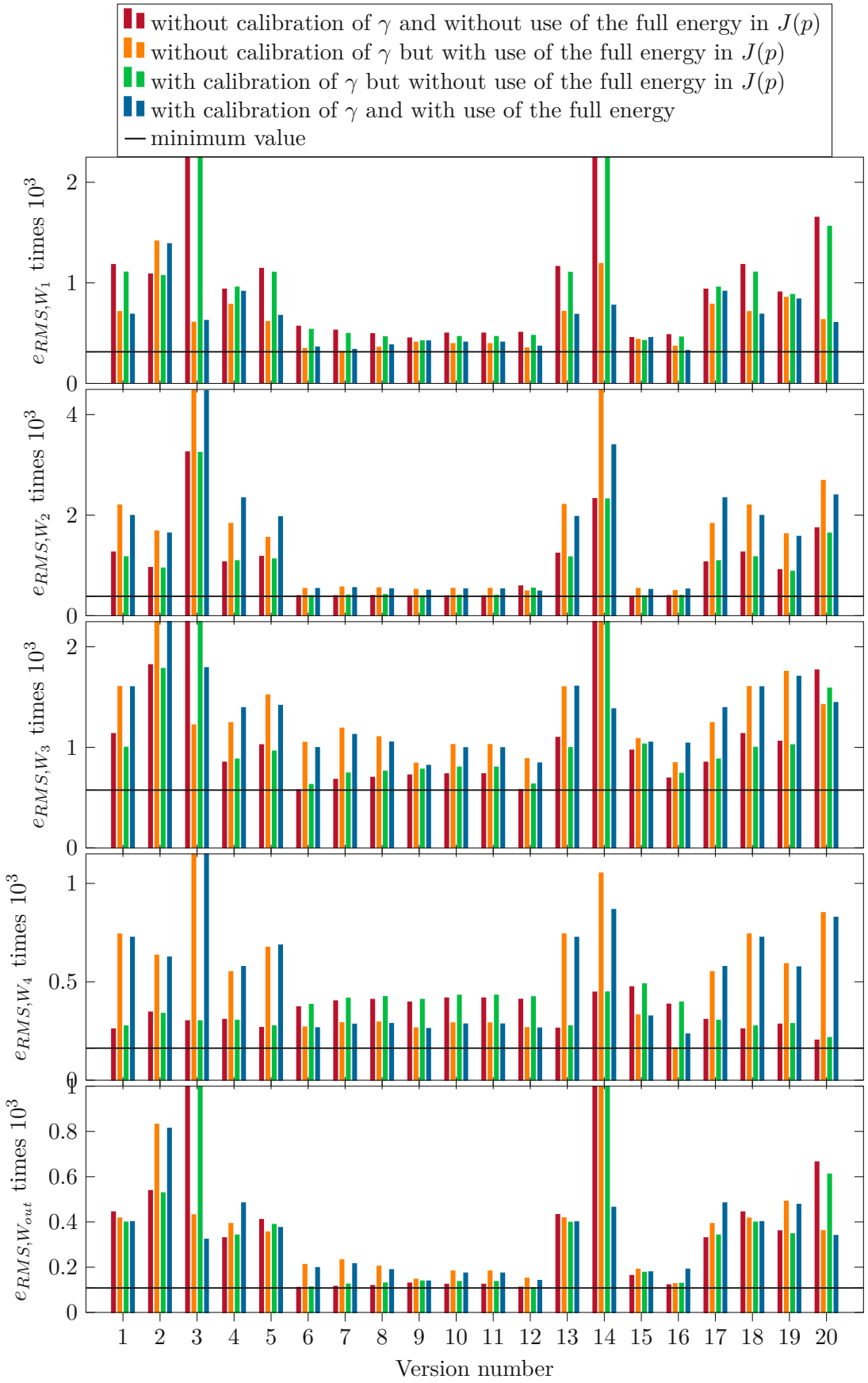

Figure A.1: Different RMS values of the split for the full energy for all calibration variants as well as the four different configurations. The lowest values is marked.

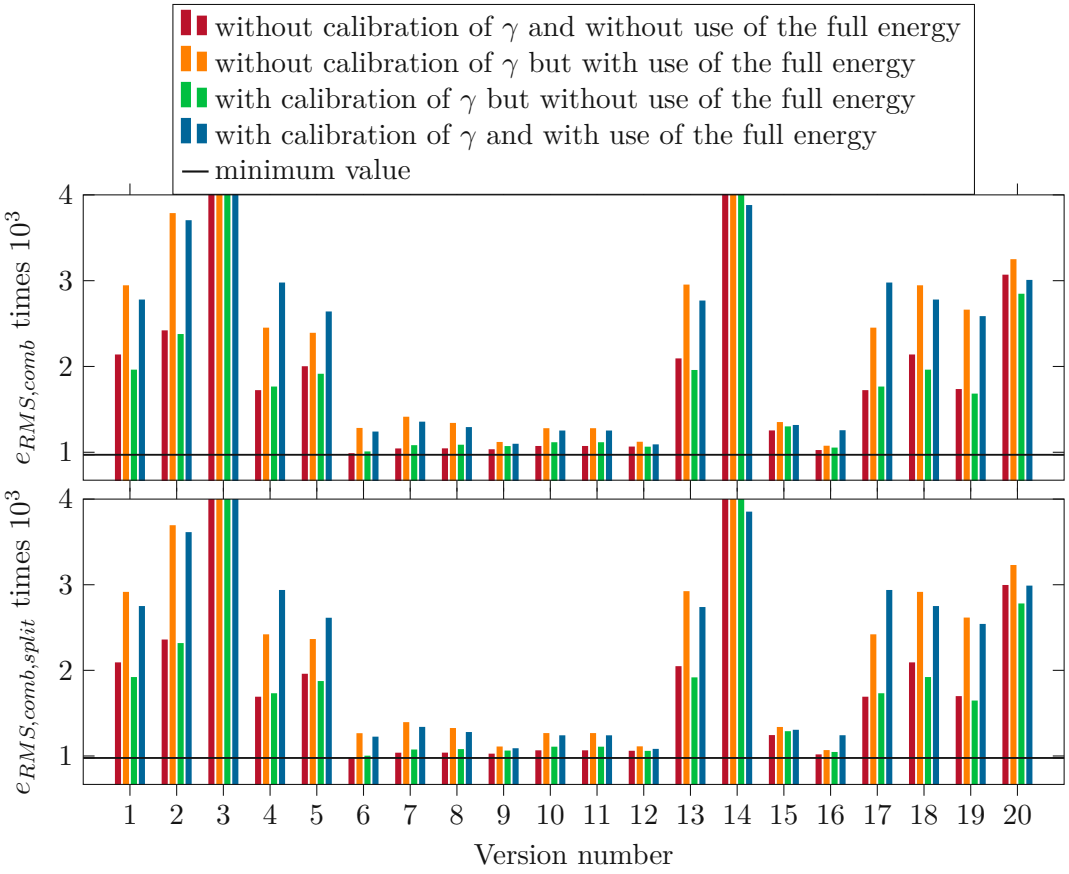

Figure A.2: Combined RMS values for all calibration variants for the four different configurations. The lowest values is marked.

Bibliography

[1] J. L. Bromberg, "The birth of the laser," *Physics today*, vol. 41, no. 10, pp. 26–33, 1973.

[2] T. Sakimoto, M. I. Rosenblatt, and D. T. Azar, "Laser eye surgery for refractive errors," *The Lancet*, vol. 367, no. 9520, pp. 1432–1447, 2006.

[3] T. Lucatorto, M. De Graef, R. F. Haglund, and J. C. Miller, *Laser Ablation and Desorption*. San Diego: Elsevier Science & Technology, 1997, vol. 30.

[4] B. S. Yilbas, *The Laser Cutting Process: Analysis and Applications*. San Diego: Elsevier, 2017.

[5] C. Yeo, S. Tam, S. Jana, and M. W. Lau, "A technical review of the laser drilling of aerospace materials," *Journal of Materials Processing Technology*, vol. 42, no. 1, pp. 15–49, 1994.

[6] R. Kodama *et al.*, "Fast heating scalable to laser fusion ignition," *Nature*, vol. 418, no. 6901, pp. 933–934, 2002.

[7] R. X. Adhikari, "Gravitational radiation detection with laser interferometry," *Reviews of Modern Physics*, vol. 86, no. 1, pp. 121–151, 2014.

[8] G. P. Agrawal, *Fiber-optic communication systems*. New York: Wiley, 2008.

[9] S. Faruque, *Free Space Laser Communication with Ambient Light Compensation*. Cham: Springer International Publishing, 2021.

[10] W. H. Lowdermilk and J. E. Murray, "The multipass amplifier: Theory and numerical analysis," *Journal ofApplied Physics*, vol. 51, no. 5, p. 2436, 1980.

[11] D. Strickland and G. Mourou, "Compression of amplified chirped optical pulses," *Optics communications a journal devoted to the rapid publication of contributions in the field of optics and interaction of light with matter*, vol. 55, no. 6, p. 447, 1985.

[12] J. Dörring, A. Killi, U. Morgner, A. Lang, M. Lederer, and D. Kopf, "Period doubling and deterministic chaos in continuously pumped regenerative amplifiers," *Optics Express*, vol. 12, no. 8, pp. 1759–1768, 2004.

[13] A. M. Weiner, "Ultrafast optical pulse shaping: A tutorial review," *Optics Communications*, vol. 284, no. 15, pp. 3669–3692, 2011.

[14] A. M. Weiner, "Femtosecond pulse shaping using spatial light modulators," *Review of Scientific Instruments*, vol. 71, no. 5, pp. 1929–1960, 2000.

[15] M. Dugan, J. Tull, and W. Warren, "High-resolution acousto-optic shaping of unamplified and amplified femtosecond laser pulses," *Journal of the Optical Society of America. B, Optical physics*, vol. 14, no. 9, pp. 2348–2358, 1997.

[16] E. Zeek *et al.*, "Pulse compression by use of deformable mirrors," *Optics Letters*, vol. 24, no. 7, pp. 493–495, 1999.

[17] P. Malevich *et al.*, "High energy and average power femtosecond laser for driving mid-infrared optical parametric amplifiers," *Optics Letters*, vol. 38, no. 15, pp. 2746–2749, 2013.

[18] F. Omenetto, D. Reitze, B. Luce, M. Moores, and A. Taylor, "Adaptive control methods for ultrafast pulse propagation in optical fibers," *IEEE Journal of Selected Topics in Quantum Electronics*, vol. 8, no. 3, pp. 690–698, 2002.

[19] P. Dower, P. Farrell, and D. Nesic, "Extremum seeking control of cascaded raman optical amplifiers," *IEEE Transactions on Control Systems Technology*, vol. 16, no. 3, pp. 396–407, 2008.

[20] S. L. Brunton, X. Fu, and J. N. Kutz, "Extremum-seeking control of a mode-locked laser," *IEEE Journal of Quantum Electronics*, vol. 49, no. 10, pp. 852–861, 2013.

[21] B. Ren, P. Frihauf, M. Krstic, and R. J. Rafac, "Laser pulse shaping via iterative learning control and high-dimensional extremum seeking," in *ASME 2011 Dynamic Systems and Control Conference and Bath/ASME Symposium on Fluid Power and Motion Control, DSCC 2011*, vol. 1, ASMEDC, 2011, pp. 667–674.

[22] A. Deutschmann, P. Malevich, A. Baltuška, and A. Kugi, "Modeling and iterative pulse-shape control of optical chirped pulse amplifiers," *Automatica*, vol. 98, pp. 150–158, 2018.

[23] D. H. Owens, *Iterative Learning Control: An Optimization Paradigm*. London: Springer, 2015.

[24] Y. Chen, C. Wen, and M. Sun, "A robust high-order p-type iterative learning controller using current iteration tracking error," *International Journal of Control*, vol. 68, no. 2, pp. 331–342, 1997.

[25] S. Riaz, H. Lin, M. Bilal Anwar, and H. Ali, "Design of pd-type second-order ilc law for pmsm servo position control," *Journal of Physics: Conference Series*, vol. 1707, no. 1, p. 12 002, 2020.

[26] D. Yoon, X. Ge, and C. E. Okwudire, "Optimal inversion-based iterative learning control for overactuated systems," *IEEE Transactions on Control Systems Technology*, vol. 28, no. 5, pp. 1948–1955, 2020.

[27] J. Ghosh and B. Paden, "A pseudoinverse-based iterative learning control," *IEEE Transactions on Automatic Control*, vol. 47, no. 5, pp. 831–837, 2002.

[28] D. Bristow, M. Tharayil, and A. Alleyne, "A survey of iterative learning control," *IEEE Control Systems*, vol. 26, no. 3, p. 96, 2006.

[29] R. W. Longman, "Iterative learning control and repetitive control for engineering practice," *International Journal of Control*, vol. 73, no. 10, pp. 930–954, 2000.

[30] M. Grishin, V. Gulbinas, and A. Michailovas, "Bifurcation suppression for stability improvement in nd:yvo4 regenerative amplifier," *Optics Express*, vol. 17, no. 18, pp. 15 700–15 708, 2009.

[31] A. Deutschmann, P. Malevich, A. Baltuška, and A. Kugi, "Identifikation und simulation optischer verstärker für ultra-kurze laserpulse," *at - Automatisierungstechnik*, vol. 66, no. 1, pp. 66–78, 2018.

[32] G. F. Franklin, J. D. Powell, and M. L. Workman, *Digital control of dynamic systems*. Menlo Park, California: Addison-Wesley, 1998.

[33] D. Simon, *Optimal state estimation : Kalman, H [infinity] and nonlinear approaches*, eng. Hoboken, N.J.: Wiley-Interscience, 2006.

[34] A. Deutschmann-Olek, G. Stadler, and A. Kugi, "Stochastic iterative learning control for lumped- and distributed-parameter systems: A wiener-filtering approach," *IEEE Transactions on Automatic Control*, vol. 66, no. 8, pp. 3856–3862, 2021.

[35] S. J. Bence, K. F. Riley, and M. P. Hobson, *Mathematical methods for physics and engineering: a comprehensive guide*. Cambridge University Press, 2012.

[36] W. Squire and G. Trapp, "Using complex variables to estimate derivatives of real functions," *SIAM Review*, vol. 40, no. 1, pp. 110–112, 1998.

Eidesstattliche Erklärung

Hiermit erkläre ich, dass die vorliegende Arbeit gemäß dem Code of Conduct – Regeln zur Sicherung guter wissenschaftlicher Praxis (in der aktuellen Fassung des jeweiligen Mitteilungsblattes der TU Wien), insbesondere ohne unzulässige Hilfe Dritter und ohne Benutzung anderer als der angegebenen Hilfsmittel, angefertigt wurde. Die aus anderen Quellen direkt oder indirekt übernommenen Daten und Konzepte sind unter Angabe der Quelle gekennzeichnet. Die Arbeit wurde bisher weder im In– noch im Ausland in gleicher oder in ähnlicher Form in anderen Prüfungsverfahren vorgelegt.

Vienna, September 2022

Nikolaus Würkner